Electrochemical pre-treatment of aluminum alloy in environmentally friendly medium: Parameter optimization and bonding strengthening mechanism

Qifan Hu[a], Zhenghui Ge[a, *], Kai Pang[b], Yongwei Zhu[a], Xiaonan Hou[b]

[a]*College of Mechanical Engineering, Yangzhou University, Yangzhou 225009, China*

[b]*Department of Engineering, Engineering Building, Lancaster University, Lancaster LA1 4YW, UK*

[*]Corresponding author: Zhenghui Ge (zhge@yzu.edu.cn)

Abstract: The electrochemical treatment of adhesive surfaces in neutral salt solutions is a promising novel method for improving the bonding performance of aluminum alloys. However, the mechanism through which this treatment improves interfacial bonding strength remains poorly understood. This study systematically investigates the relationship among electrochemical parameters, microstructure, property evolution, and the bonding strength of thin-walled aluminum adhesive joints. Multi-scale characterization techniques were employed to elucidate the strengthening mechanism from the perspectives of chemical bonding and mechanical interlocking. The results demonstrated that a current density of 0.8 $A \cdot cm^{-2}$ applied for 100 s increased the bonding strength by 170% compared to untreated joints. Furthermore, the effect of electrochemical treatment, sandblasting, and grinding on the surface characteristics and bonding properties was compared. XPS and FTIR analyses revealed that the electrochemical treatment significantly increased the surface density of hydroxyl groups, which promoted the opening of epoxy rings and the subsequent formation of covalent bonds. This finding confirms the critical role of chemical bonding in enhancing interfacial strength. Eventually, a qualitative model was developed to illustrate the mechanism by which electrochemical treatment enhances the adhesive performance of aluminum alloy joints. These insights are valuable for exploring the potential application of electrochemical treatment to thin-walled, lightweight alloy components.

Keywords: Adhesive bonding; Aluminum alloy; Single lap joint; Electrochemical treatment; Interfacial chemical bonding

1. Introduction

Thin-walled aluminum alloy components are extensively utilized in aerospace, automotive, and rail transportation applications, such as aircraft fuselages, wings, and automobile body frames, due to the requirements for large spans, high specific strength, and light weight [1–3]. Conventional joining techniques, such as riveting and welding, often introduce issues like stress concentration, thermal deformation, and compromised structural integrity. In contrast, adhesive bonding technology has become a pivotal technique for assembling thin-walled structures, offering benefits such as uniform stress distribution and continuous bonding surfaces [4-7]. However, the inherent dense oxide layer on aluminum alloys reduces surface energy and weakens chemical reactivity, thereby impairing adhesion at the bonded interface [8,9]. Consequently, surface pre-treatment is commonly used in industry to improve the surface characteristics of aluminum alloy and achieve robust bonding strength [10-12].

Industrial pre-treatment methods for bonding surface preparation commonly include mechanical [13], physical [14], and chemical treatments [15]. Traditional mechanical processes, such as grinding and sandblasting, remain essential for enhancing surface adhesion. They achieve this by increasing surface roughness to improve mechanical interlocking, which subsequently enhances bonding strength [16-18]. However, research indicates that the relationship between surface roughness and joint strength is not linear. Beyond a certain threshold, further increases in roughness have a diminishing effect on bonding strength [19,20]. Therefore, relying solely on the surface roughness originated from mechanical treatment is insufficient to achieve the desired bonding performance in industrial applications.

Physical treatment techniques, including laser, plasma, and discharge treatments, have gained interest for achieving high adhesive strength [21-23]. These treatments enhance bonding properties by altering surface morphology at both microscopic and macroscopic scales [24-27]. Such modifications not only reduce stress concentration and enhance mechanical interlocking but also improve surface hydrophilicity and energy. The synergy between morphological control and surface modification enhances bonding strength, making these techniques more effective than traditional mechanical

treatments. However, techniques like laser and plasma treatment require sophisticated equipment and incur high costs, posing significant challenges [28,29].

Chemical treatments, including cleaning, etching, and anodizing, offer advantages such as process simplicity, ease of operation, and low equipment costs. Chemical cleaning removes oxide layers and impurities from substrates using acidic or alkaline solutions [30-31]. This process cleans and activates the bonding surface, thereby enhancing bond strength. For instance, Prolong et al. [32] used a mixture of 10% sulfuric acid and 20% ferrous sulfate to clean an aluminum alloy surface, which improved wettability and increased bonding strength. Similarly, Joshi et al. [33] applied alkaline solutions to remove a magnesium-rich oxide layer from an aluminum alloy, resulting in significantly improved adhesive bonding strength.

Chemical etching modifies the microstructure of metal surfaces to regulate surface roughness and enhance adhesive bonding strength. For instance, Saleema et al. [9] used a NaOH solution to create a rough micro-texture on a substrate surface, increasing adhesive bonding strength by approximately 60%. Similarly, Pierre et al. [34] produced a brush-shaped microstructure through chemical etching, which doubled the joint strength. These studies demonstrate that chemical treatments, including cleaning and etching, can improve adhesive bonding properties. However, challenges such as long processing times [35] and the use of hazardous acid or alkali solutions limit their application [36-38].

Anodizing is a widely used chemical treatment for bonding surface preparation. Solutions of H_2CrO_4 and H_3PO_4 are commonly employed as electrolytes because they promote the formation of highly porous oxide films [39, 40]. For example, Zhang et al. [41] created a porous oxide layer on an aluminum alloy surface by anodizing in an H_2CrO_4 bath, which enhanced the mechanical interlocking between the adhesive and the substrate. Similarly, Dong et al. [42] altered the fracture mode of single-lap joints (SLJs) by optimizing anodizing parameters in an H_3PO_4 solution, concluding that generating sufficient micro-pores on the surface is essential for improving bond strength. However, electrolytes such as H_2CrO_4 and H_3PO_4 can release carcinogenic compounds during anodizing, posing significant health risks [43, 44].

Electrochemical treatment in neutral salt solutions presents a promising approach for enhancing the bonding properties of aluminum alloy surfaces, offering advantages over conventional chemical methods. This technique is notable for its cost-effectiveness, high efficiency, and ability to produce robust bonds. Furthermore, it is user-friendly, operationally simple, and environmentally sustainable. Preliminary research has demonstrated that aluminum alloy specimens treated in a NaCl solution for 60 s exhibit significantly improved surface roughness and wettability compared to untreated specimens. Consequently, the bonding strength of electrochemically treated specimens more than doubles. These findings indicate significant effectiveness and broad application potential for this method in improving aluminum alloy adhesion. However, the mechanisms through which electrochemical treatment enhances interfacial bonding strength remain insufficiently explored.

This study systematically investigates the relationships between electrochemical parameters, resulting surface characteristics, and ultimate bonding performance. The impact of current density and duration during the electrochemical treatment on the surface properties (e.g., roughness and hydrophilicity) of aluminum alloy and its corresponding bonding strength was thoroughly analyzed. Additionally, three treatment methods, including electrochemical treatment, sandblasting, and grinding, are introduced, and their effects on surface properties and bonding strength are comparatively analyzed. Multi-scale characterization techniques, including SEM, laser confocal microscopy, XPS, and FTIR, were employed to elucidate the contribution of chemical bonding to the overall adhesive strength. This research aims to provide experimental evidence and theoretical support for expanding the engineering application of electrochemical treatment in thin-walled lightweight alloy components.

2. Experimental

2.1. Materials and sample preparation

The specimens were fabricated from a 3 mm thick 6082-T6 aluminum alloy sheet, and its chemical composition is listed in Table 1. Loctite EA 9497 adhesive was used, with a base viscosity of 5-16 Pa·s and a hardener viscosity of 8-24 Pa·s. The adhesive was cured at room temperature. Tensile tests were performed on both the AA 6082-T6

sheet and the adhesive according to EN 485-2:2016 and ISO 527-2:2012 [45,46], respectively. The resulting mechanical properties are presented in Table 2 [47,48].

Table 1
Chemical composition of untreated AA6082-T6.

Material	Elemental composition (wt.%)								
	Si	Fe	Cu	Mn	Mg	Zn	Ti	Cr	Al
AA6082-T6	0.82	0.22	0.02	0.53	0.64	0.02	0.01	0.01	97.73%

Table 2
The bulk property of adherends and adhesives.

Property	Al 6082	Loctite EA 9497
Young Modulus (GPa)	70.77±0.385	7.70535±0.46808
Yield Stress (MPa)	254.59±3.20	46.29±3.13
Elongation at fracture (%)	10.83±0.95	0.71±0.09
Poisson Ratio	0.30±0.01	0.29
Density (kg/m^3)	2700	1100

The single lap test is a standard method for evaluating the strength of adhesive joints [3]. Consequently, single-lap joints (SLJs) were used in this study to assess the influence of electrochemical parameters on the bonding strength of AA 6082-T6. As shown in Fig. 1, the Loctite EA 9497 adhesive was applied to the electrochemically treated substrate surface after ultrasonic cleaning. Short copper wires with a diameter of 0.2 mm were evenly distributed within the adhesive layer to act as spacers, controlling its thickness. The bonded specimens were then cured at room temperature for seven days to ensure complete bonding. All SLJs were manufactured with identical dimensions based on the industry standard BS ISO 4587:2003 [49] and previous studies [50,51]. The key dimensions were as follows: adherend length (L) of 100 mm, adherend thickness (t_s) of 3 mm, adhesive thickness (t_a) of 0.2 mm, joint width (W) of 25 mm, and overlap length (L_s) of 25 mm. Two square tabs, each with a side length (L_t) of 25 mm, were bonded to the ends of the joints to mitigate bending moments and ensure precise alignment during testing.

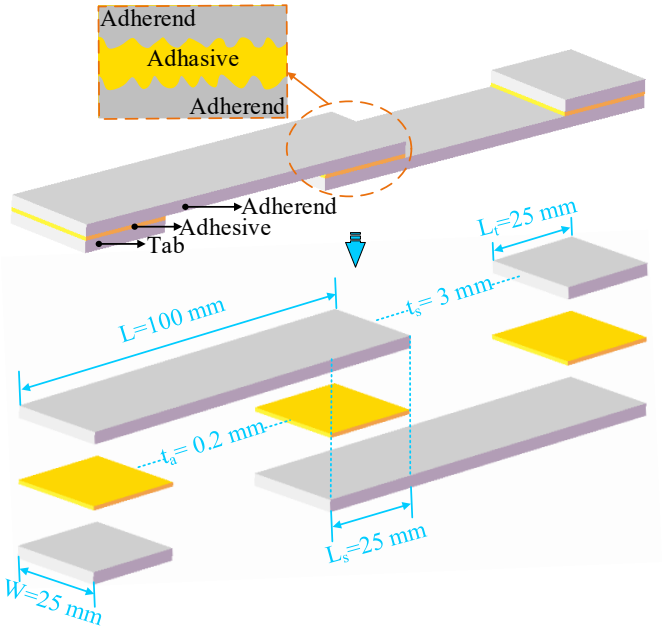

Fig. 1. Structure and geometry dimensions of the SLJs.

2.1.1 Electrochemical treatment parameters and strategies

Fig. 2 shows the schematic of the electrochemical treatment setup, which comprised an aluminum substrate (working electrode), a stainless-steel counter electrode, an insulating shield, and an electrolyte tank. The aluminum specimens and stainless-steel electrode were immersed in the electrolyte at a fixed distance. An external power supply established the electric field, while custom shielding plates precisely defined the surface treatment area on the specimens.

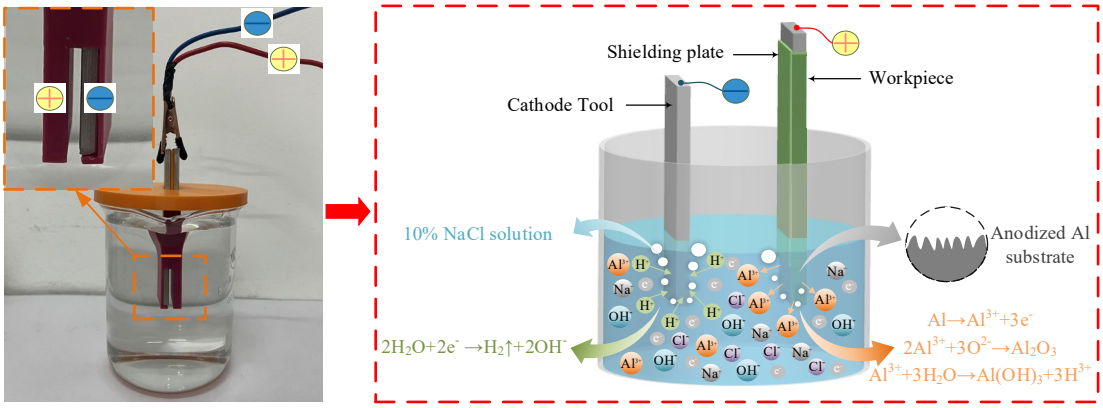

Fig. 2. Schematic diagram of the electrochemical treatment process for Al alloy joints.

A neutral electrolyte (10% sodium chloride solution), validated in prior research for its environmental compatibility and experimental efficacy, was used as the processing medium [52]. A large batch of electrolyte was prepared to ensure consistent initial conditions, with a 400 mL aliquot used for each experimental run. To mitigate

pH variation, the electrolyte was replaced after processing each sample, ensuring all samples were exposed to a similar pH environment (pH 7.03-7.6).

Before electrochemical treatment, the aluminum alloy substrates underwent sequential ultrasonic cleaning in water, ethanol, and again in water to remove surface grease and impurities thoroughly. A stepwise strategy was employed to optimize the electrochemical parameters. First, single-variable experiments were conducted to identify the optimal current density range. Subsequently, the treatment duration was optimized based on these initial findings. The complete sets of process parameters and optimization pathways are detailed in Tables 3 and 4.

Table 3
Current intensity one-factor gradient optimization parameters.

Item	Parameters							
Current density ($A \cdot cm^{-2}$)	0	0.16	0.48	0.8	1.12	1.44	1.76	2.08
Time (s)	0	60	60	60	60	60	60	60

Table 4
Time one-factor gradient optimization parameters.

Item	Parameters											
Time (s)	0	20	40	60	80	100	120	150	180	210	240	270
Current density ($A \cdot cm^{-2}$)	0	0.8	0.8	0.8	0.8	0.8	0.8	0.8	0.8	0.8	0.8	0.8

2.1.2 Mechanical processing

The reference surfaces were prepared by mechanical grinding and sandblasting, respectively. During the grinding process, a normal load was applied manually and simultaneously to both sides of each specimen. Surface roughness was monitored periodically using a portable roughness tester (SJ-210, Japan) until the average roughness (R_a) reached the target range. The sandblasted specimens were then subjected to rigorous roughness testing to confirm compliance with predefined specifications. Finally, all pre-treated specimens underwent a sequential ultrasonic cleaning procedure in water, ethanol, and again in water to ensure complete removal of surface residues.

2.2 Surface characterization and performance testing

2.2.1 Surface microstructure characterization

The specimen surfaces were characterized using scanning electron microscopy

(SEM, GeminiSEM 300 FESEM, Carl Zeiss Microscopy GmbH, Germany), and the resulting images were analyzed with ImageJ software. Three-dimensional surface topography was assessed using a white light interferometer (WLI, ContourGT-K, Bruker, USA). The raw 3D data were processed with Vision64 software for plane correction and parameter extraction, yielding key topographic parameters such as the 3D surface map and the arithmetic mean height (S_a).

2.2.2 Wettability test

The contact angle (CA) of a water droplet on the specimen surface was measured at room temperature using a contact angle measuring system (ZJ7000, Shenzhen, China), as shown in Fig. 3. For each specimen, three measurements were taken within 24 hours of surface treatment using 2 μL droplets of distilled water and diiodomethane. A larger spreading extent of the liquid on the surface indicates stronger wettability, while a smaller extent suggests poorer wettability. The surface free energy (SFE) of the aluminum alloy specimens before and after treatment was calculated using the Owens-Wendt-Rabel-Kaelble (OWRK) method. The SFE comprises dispersive and polar components, as expressed in Eq. (1). The surface tension components of the test liquids are listed in Table 5.

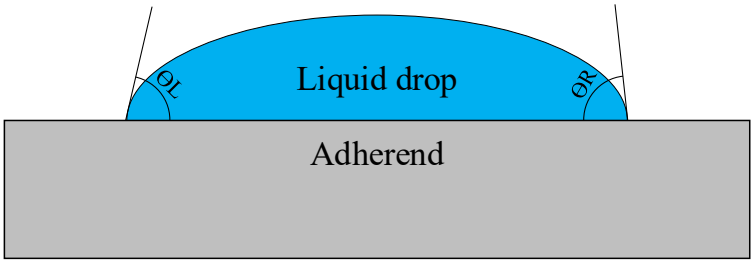

Fig. 3. Schematic diagram of CA measurement.

$$\gamma_S = \gamma_S^D + \gamma_S^P \tag{1}$$

where γ_S denoted the solid SFE calculated from Eq. (1), γ_S^D denoted the dispersion component of the solid SFE, and γ_S^P denoted the polar component of the solid SFE. Values of γ_S^D and γ_S^P were calculated from Eqs. (2) and (3).

$$\gamma_{LW}\left(1+\cos\theta_W\right) = 2\left(\gamma_S^D\gamma_{LW}^D\right)^{\frac{1}{2}} + 2\left(\gamma_S^P\gamma_{LW}^P\right)^{\frac{1}{2}} \tag{2}$$

$$\gamma_{LD}\left(1+\cos\theta_D\right)=2\left(\gamma_S^D\gamma_{LD}^D\right)^{\frac{1}{2}}+2\left(\gamma_S^P\gamma_{LD}^P\right)^{\frac{1}{2}} \tag{3}$$

where γ_{LW} denoted the SFE of water, θ_W denoted the measured CA of water, γ_{LW}^D denoted the disperse component of the water SFE, γ_{LW}^P denoted the polar component of the water SFE, γ_{LD} denoted the SFE of diiodomethane, θ_B denoted the measured CA of diiodomethane, γ_{LD}^D denoted the disperse component of the diiodomethane SFE, and γ_{LD}^P denoted the polar component of the diiodomethane SFE.

Table 5
Surface tension components of the test liquids (mJ/m^2).

Liquid	γ_L	γ_L^D	γ_L^P
Water	72.8	21.8	51
Diiodomethane	50.8	50.8	0

2.2.3 Surface chemical composition and molecular structure characterization

The chemical composition of the outermost layer of the aluminum alloy specimens before and after electrochemical treatment was analyzed by X-ray photoelectron spectroscopy (XPS, ESCALAB 250Xi, Thermo Fisher Scientific Inc., USA). Survey spectra were acquired with a pass energy of 150 eV and a step size of 1 eV in constant analyzer energy (CAE) mode. All samples were analyzed via narrow-scan spectroscopy within 24 hours after the electrochemical treatment. Elemental atomic concentrations were calculated based on the spectral peak areas and the sensitivity factor. Data analysis was performed using Avantage software, with the binding energy scale referenced to the adventitious carbon C 1s peak at 284.8 eV. Fourier transform infrared spectroscopy (FTIR, Nicolet iS20, USA) was used to characterize the chemical structure of the adhesive interface. Spectra were recorded from 4000 to 400 cm^{-1} with a resolution of 4 cm^{-1} and 32 scans per spectrum.

2.2.4 Tensile shear test

All quasi-static uniaxial tensile tests were performed on an Instron 3380 universal testing machine with a 100 kN load cell. Tests were conducted in displacement control at a constant rate of 0.5 mm/min. The load was applied tangentially to the adhesive

interface until joint failure, and the maximum load (F_{max}) was recorded. The average shear strength (τ) was calculated as the ratio of F_{max} to A, where A is the bonded area in the lap region ($A = L_s \times W$, with L_s being the overlap length and W the specimen width). For each configuration, five replicate specimens were tested to failure to obtain the stress-displacement curves. An Imetrum video gauge system was used to monitor displacement during testing, as illustrated in Fig. 4(a). A grid of black dots was applied to the overlap region to serve as high-contrast markers, while a ruler was affixed next to the SLJ for dimensional calibration. The system tracked marker movement to determine joint displacement from the vertical separation between reference points 1 and 2 (red markers). Fig. 4(b) presents three characteristic failure modes of SLJs after tensile testing. Mixed and cohesive failures are identified as the preferred mechanisms, indicating favorable adhesive properties of the substrate materials.

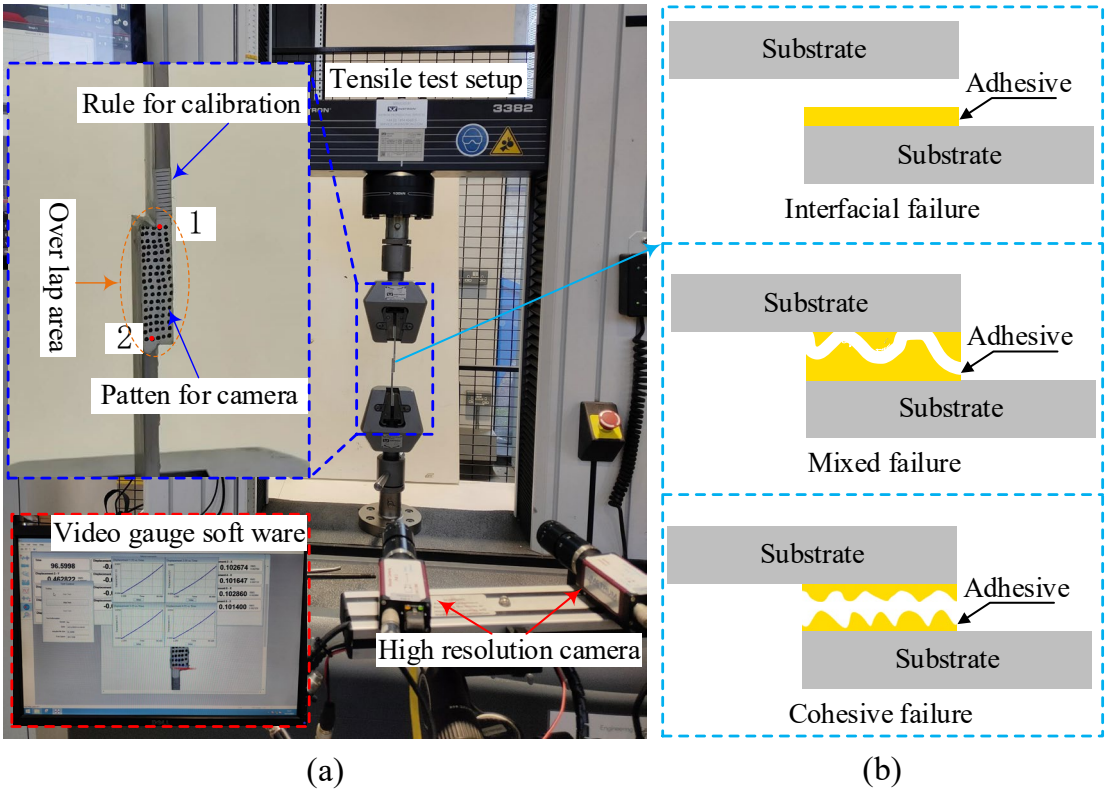

Fig. 4. Tensile testing device (a) and three typical fracture (b) forms of SLJs.

3. Results and analyses

3.1. Effect of current density on surface characteristics and bonding strength

Fig. 5 shows the surface morphology of aluminum alloy specimens before and after electrochemical treatment at various current densities. The untreated surface

exhibited parallel grinding scratches with grooves (Fig. 5(a)). At 0.16 A·cm⁻², discrete corrosion pits appeared, retaining approximately 82.8% of the initial texture (Fig. 5(b)), indicating that corrosion was dominated by local pitting, with the passivation layer remaining intact. As the current density increased to 0.48 A·cm⁻², pitting expanded, and texture retention decreased to 12.6% (Fig. 5(c)). When the current densities exceeded 0.8 A·cm^{-2}, the surface began to exhibit a uniform corrosion morphology, and the original grinding texture almost disappeared (Fig. 5(d)). Further increases to 1.12 and 1.44 A·cm⁻² led to more intense corrosion (Fig. 5(e)-(f)). At 1.76 and 2.08 A·cm⁻², no initial texture remained, and the surface exhibited a smoother, homogeneous morphology, suggesting complete removal of the original structure. These results demonstrate a transition from local pitting to uniform corrosion with increasing current density, accompanied by passivation layer destruction and texture loss, which may cause significant variation in S_a.

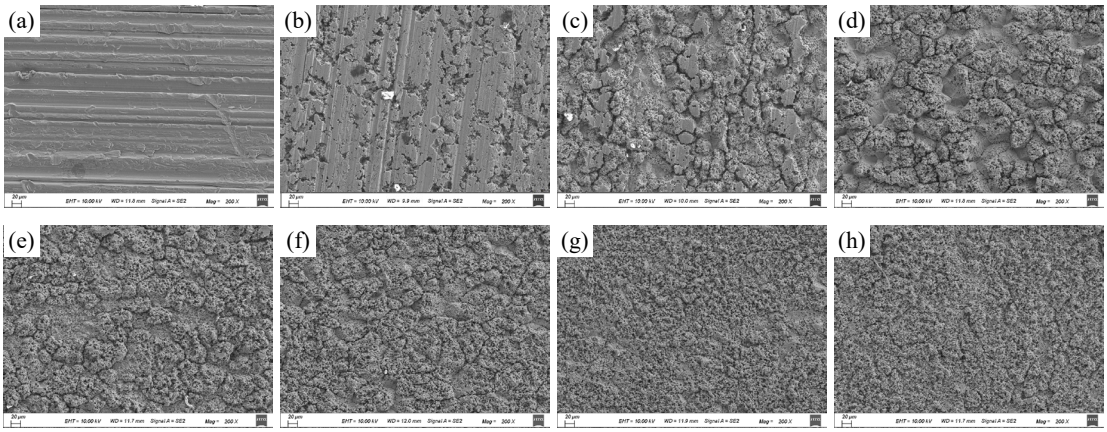

Fig. 5. Surface morphology of aluminum alloy specimens under different current densities, (a)-(h) correspond to the surface morphology of specimens with current densities of 0, 0.16, 0.48, 0.8, 1.12, 1.44, 1.76, and 2.08 A·cm^{-2}, respectively.

The 3D surface morphology and S_a of the specimens under different current densities were characterized using WLI, as shown in Fig. 6. The untreated surface had distinct grinding scratches with an S_a of 2.88 μm (Fig. 6(a) and (i)). S_a increased with current density, reaching a maximum of 4.088 μm at 0.8 A·cm⁻², representing a 41.9% increase from the initial value (Fig. 6(d) and (i)), corresponding to the most complex morphology. Beyond this point, S_a decreased, and the surface became more uniform. At 1.76 A·cm⁻², S_a fell below the initial level (Fig. 6(g), (h), and (i)). Therefore, S_a initially increased and then decreased with current density, which can be ascribed to the

shift from localized pitting to homogeneous corrosion mechanisms.

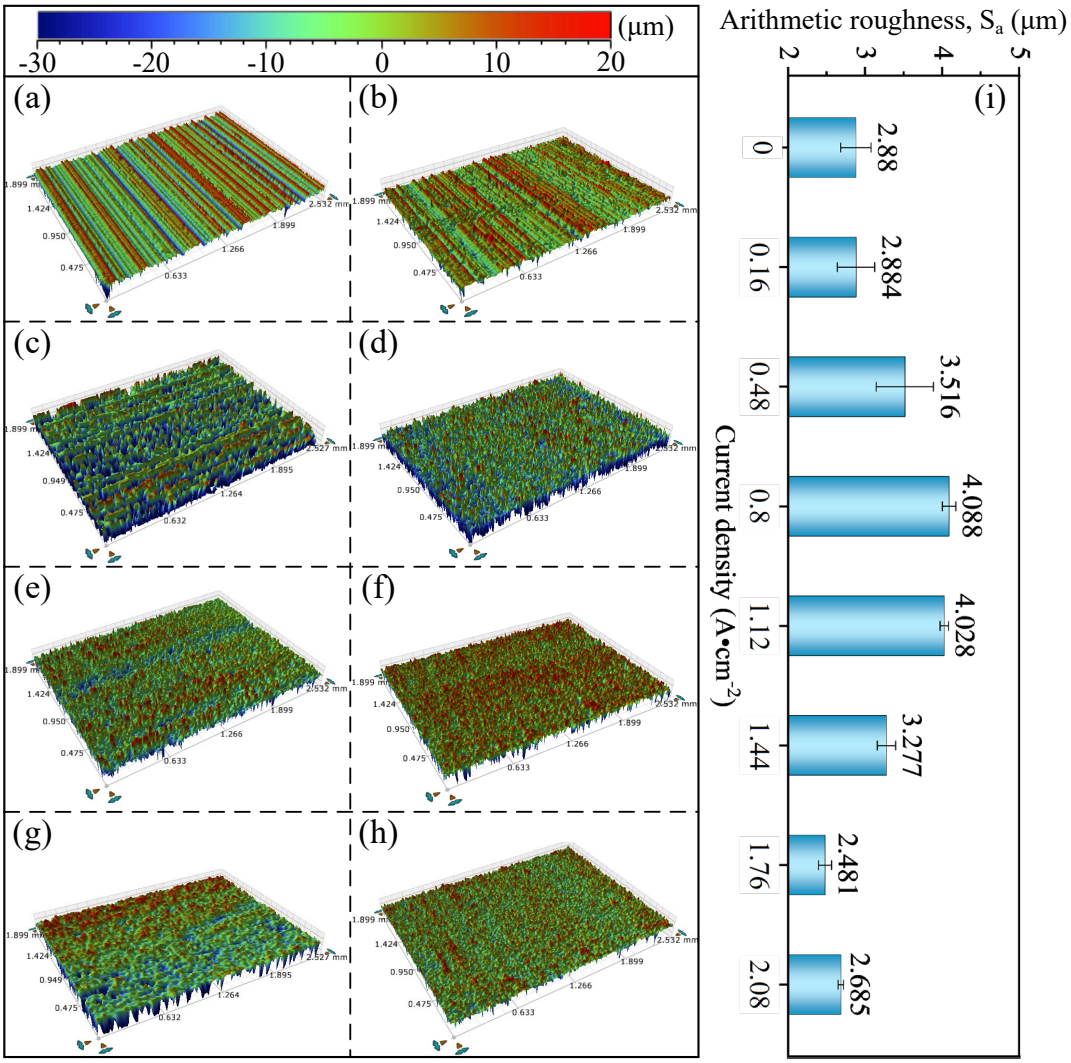

Fig. 6. 3D surface morphology and S_a of aluminum alloy specimens at different current densities, (a)-(h) correspond to the surface state of the specimens at current densities of 0-2.08 A·cm^{-2}, respectively, and (i) is the S_a.

Fig. 7 shows the CA tests performed on treated specimens with varying current densities. The water CA on untreated surfaces was 90.2°, indicating poor wettability (Fig. 7(a1)). CA decreased with current density, dropping to 32° at 0.16 A·cm^{-2} (Fig. 7(b1)), and further to 19° and 11.6° at 0.48 and 0.8 A·cm^{-2}, respectively (Fig. 7(c1) and (d1)). Although a slight increase occurred at 1.44 A·cm^{-2} (Fig. 7(f1)), CA variations at high current densities were minimal, reaching 8.8° at 2.08 A·cm^{-2} (Fig. 7(h1)). These results confirm enhanced hydrophilicity with higher current density.

Diiodomethane CA showed a similar trend, as shown in Fig. 7(a2)-(h2). The CA decreased from 47.5° on untreated surfaces to 25.6° at 0.16 A·cm^{-2} and 9.7° at 2.08

A·cm⁻². Electrochemical treatment improved wettability, with the effect most pronounced at low current densities and diminishing above 0.8 A·cm⁻².

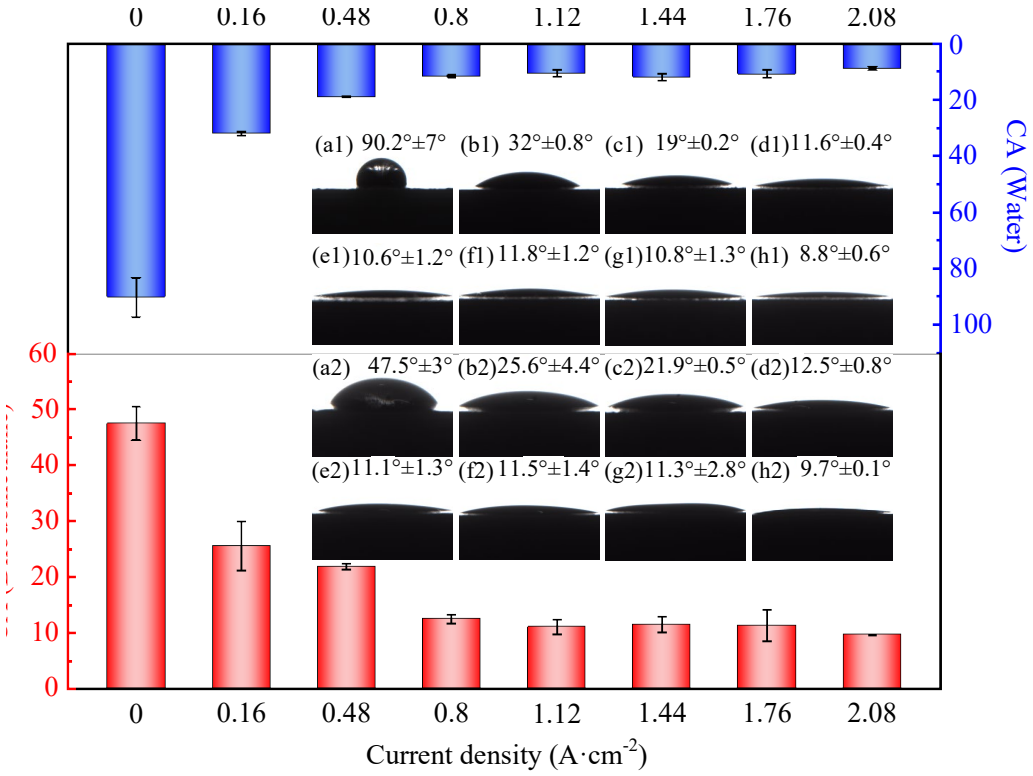

Fig. 7. CA of (a1)-(h1) water and (a2)-(h2) diiodomethane on the surface of the specimens under different current density treatment conditions, (a)-(h) corresponding to current densities of 0-2.08 A·cm^{-2}, respectively.

The SFE (γ_s) and its components (γ_s^D and γ_s^P) of aluminum alloy specimens were determined at different current densities using the OWRK method, as presented in Table 6. The SFE of the untreated specimen surface was 37.037 mJ/m², whereas that of the specimen electrochemically treated at 0.16 A·cm⁻² reached 70.819 mJ/m². The components also increased from 35.656 and 1.381 mJ/m² to 45.935 and 24.883 mJ/m², respectively. Subsequently, both the SFE and its components gradually increased with increasing current density. However, at current densities above 0.8 A·cm⁻², the change in SFE was minimal, indicating that the increase plateaued within the range of 0.8 to 2.08 A·cm⁻². It was assumed that, although surface morphology continued to change at current densities exceeding 0.8 A·cm⁻², the density of surface polar functional groups might dominate the SFE level compared to morphology. Consequently, the SFE remained consistently high as the surface polar functional groups approached saturation

at higher current densities.

The CA and SFE tests demonstrated that current density significantly affects the wettability and SFE of aluminum alloys. Both SFE and wettability increased gradually with current density. Although the changes in wettability and SFE were more gradual at higher current densities (above 0.8 A·cm^{-2}), the overall trend confirmed that electrochemical treatment positively influenced the surface properties. This suggests that adhesives can spread more effectively on treated surfaces, thereby enhancing bonding properties.

Table 6

The OWRK method is used to derive γ_S^D, γ_S^P, and γ_S (mJ/m^2) values for aluminum alloy specimens at different current density conditions.

Treatments	γ_S^D	γ_S^P	γ_S
As-received	35.656	1.381	37.037
0.16 A·cm^{-2}	45.935	24.883	70.819
0.48 A·cm^{-2}	47.200	29.426	76.626
0.8 A·cm^{-2}	49.602	30.088	79.691
1.12 A·cm^{-2}	49.854	30.148	80.002
1.44 A·cm^{-2}	49.785	29.956	79.741
1.76 A·cm^{-2}	49.819	30.129	79.949
2.08 A·cm^{-2}	50.076	30.332	80.408

Fig. 8 shows the average shear strength of SLJs after treatment at different current densities. The untreated joint, with an average shear strength of 4.16 MPa, served as the reference. Shear strength increased with current density, reaching 4.87 MPa at 0.16 A·cm^{-2} and further 6.28 MPa at 0.48 A·cm^{-2}, approximately 51% higher than that of untreated joints. Notably, after treatment at 0.8 and 1.12 A·cm^{-2}, shear strength reached 9.35 MPa and 8.74 MPa, respectively, representing an increase of over 110% compared to untreated specimens. This substantial improvement may be attributed to the increased surface roughness S_a, which enlarges the effective bonding area and enhances the mechanical interlocking effect [53]. As shown in Fig. 6, S_a increased from 2.88 μm for untreated specimens to 4.088 μm and 4.028 μm for specimens treated at 0.8 and 1.12 A·cm^{-2}, respectively. However, excessively rough surfaces can trap air bubbles during electrochemical processing, leading to inadequate wetting and reduced joint

strength [54]. Notably, CA decreased significantly and SFE increased markedly in treated specimens compared to initial ones, as evidenced by Fig. 8 and Table 6. Moreover, CA and SFE varied only slightly when current density exceeded 0.8 A·cm^{-2}. This mitigated the negative effects of excessive roughness on joint performance. Voids caused by surface roughness were filled with adhesive due to low CA, improving bonding reliability. However, at 1.44 A·cm^{-2}, joint strength decreased moderately to 7.78 MPa. At higher current densities (1.76 and 2.08 A·cm^{-2}), strength remained similar to that at 1.44 A·cm^{-2}, indicating stabilization under elevated current conditions. The strength reduction between 0.8 and 1.44 A·cm^{-2} may be due to decreased surface roughness. In contrast, the stability at 1.44 and 1.76 A·cm^{-2} suggests potential contributions from improved surface chemical forces, as roughness decreased from 3.28 μm to 2.48 μm.

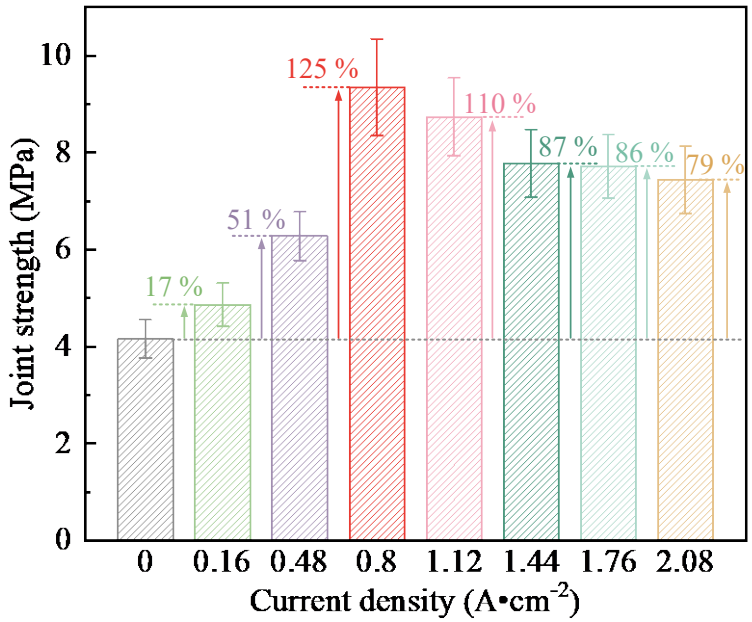

Fig. 8. The average shear strength of SLJs after treatment with different current densities.

3.2 Effect of treatment time on surface characteristics and bonding strength

Fig. 9 illustrates the morphological characteristics of aluminum alloy specimen surfaces under different treatment durations at a current density of 0.8 A·cm^{-2}. Fig. 9(a) shows the untreated specimen with distinct grinding scratches, while Figs. 9(b)-(l) depict the time-dependent evolution of the surface morphology. The images revealed a progressive increase in corrosion depth and density with prolonged treatment time, accompanied by significant morphological changes. After 20 s of treatment, the surface

predominantly exhibited micro-pits, as shown in Fig. 9(b). As treatment progressed to 40-100 s, intensified corrosion led to the gradual disappearance of grinding scratches, resulting in a complex and rough morphology (Figs. 9(c)-(f)). At the 120-270 s stage, grinding scratches were entirely removed, and the corroded surface became more uniform (Figs. 9(g)-(l)).

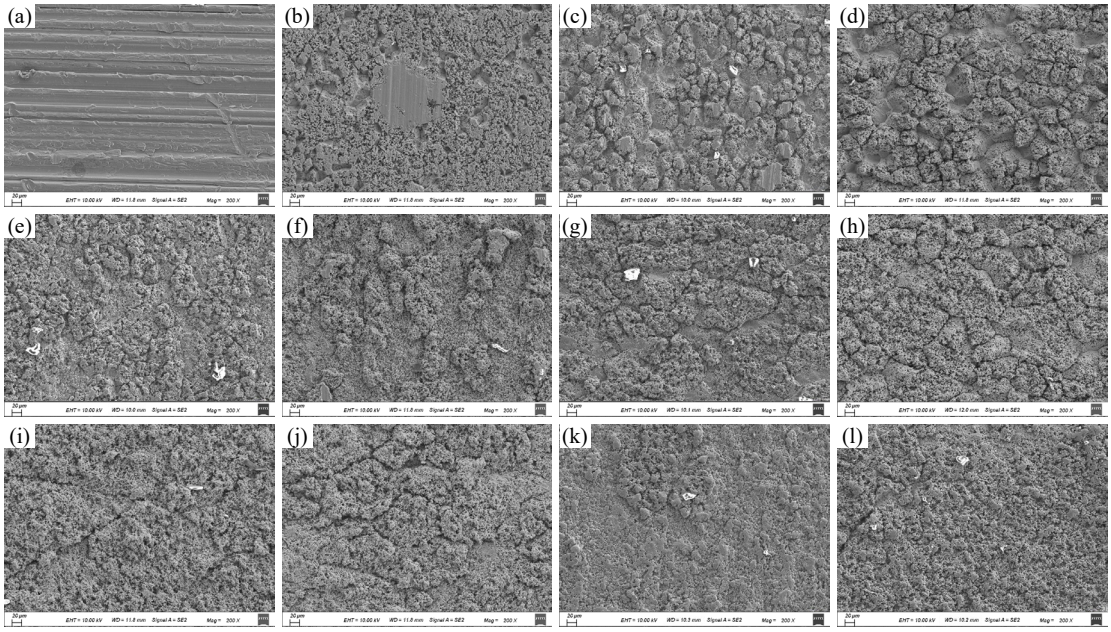

Fig. 9. Surface morphology of aluminum alloy specimens under different treatment times, (a)-(l) correspond to the surface morphology of specimens with treatment times of 0, 20, 40, 60, 80, 100, 120, 150, 180, 210, 240, and 270 s, respectively.

The 3D surface morphology and S_a of the substrate under different treatment durations were characterized using WLI, as shown in Fig. 10. Results show that S_a values initially increase, followed by a gradual decrease. After 20 s of treatment, the initial grinding texture remains visible, and S_a increases slightly. During 40-100 s, intensified corrosion becomes evident, marked by the progressive obliteration of grinding scratches and the development of a complex, rough morphology. S_a reaches above 4 μm in this phase. This evolution can be attributed to the selective etching mechanism of electrochemical corrosion, where localized regions with heterogeneous compositions or micro-defects exhibit elevated electrochemical activity, serving as preferential dissolution sites. The generation and propagation of corrosion pits in these zones induce rapid surface roughening [55-57]. Furthermore, Figs. 10(g)-(l) reveal that the grinding texture is entirely removed, the corroded surface gradually homogenizes,

and S_a decreases to approximately 3.5 μm as treatment duration increases from 120 to 240 s. The process can be summarized as the generation, expansion, and merging of micro-pits. Initially, numerous micro-pits generate and grow, increasing surface roughness, while scratches disappear. In the second stage, some micro-pits merge, leveling the surface and decreasing roughness, although new micro-pits continue to form and grow. When merging and generation reach equilibrium, surface roughness stabilizes.

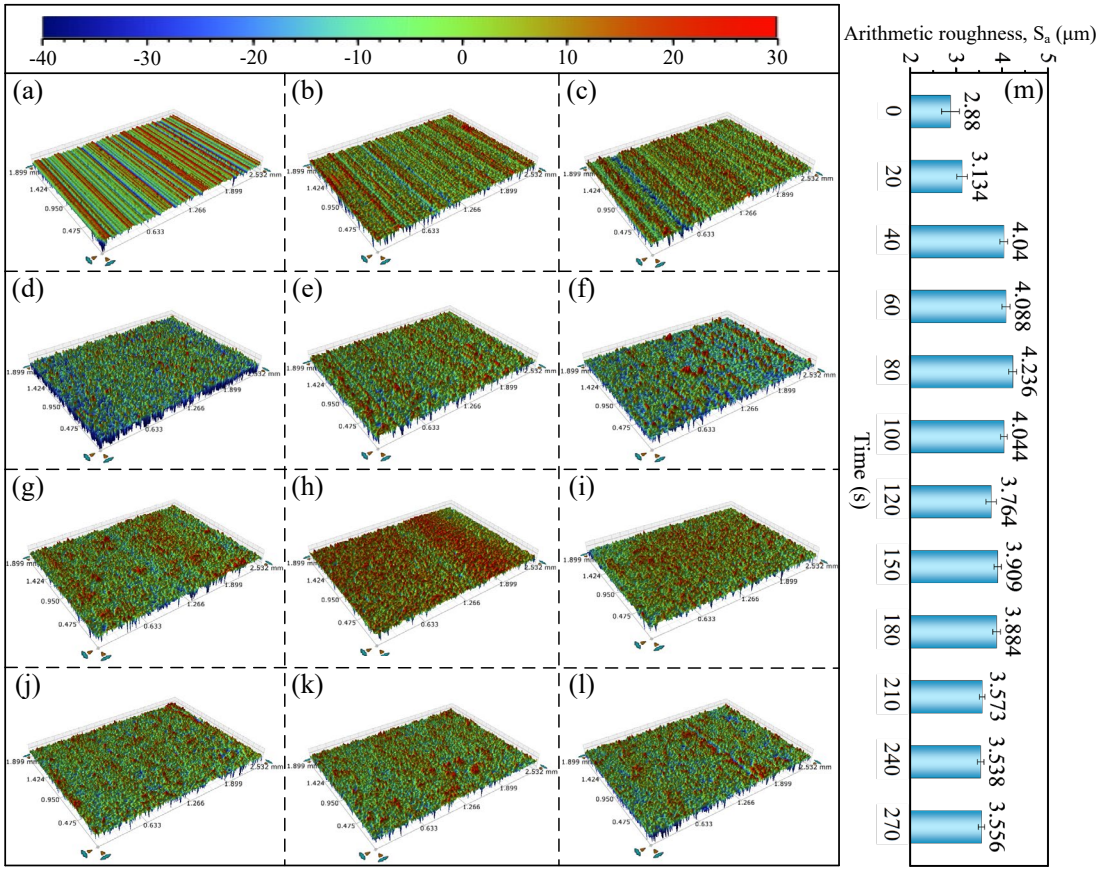

Fig. 10. 3D surface morphology and (S_a) of aluminum alloy specimens at different treatment times, (a)-(l) correspond to the surface state of the specimens at treatment times of 0-270 s, respectively, and (m) is the S_a.

Fig. 11(a1)-(l1) shows the variation in water droplet CA on the specimen surface with increasing treatment duration. The CA generally decreased, indicating enhanced surface hydrophilicity with longer treatment times. The untreated surface was hydrophobic, with an average CA of 90.2° (Fig. 11(a1)). After 20 s of treatment, the CA dropped to 35.1°, indicating a transition to hydrophilic properties (Fig. 11(b1)). Subsequently, the CA decreased to approximately 10° over the next 60 s (Fig. 11(c1)-

(e1)). During the remaining treatment period, the CA remained low (Fig. 11(f1)-(l1)), with the minimum value of 6.1° at 180 s, demonstrating the best hydrophilicity.

Fig. 11(a2)-(l2) shows the CA of diiodomethane on the aluminum alloy surface varying with the prolonged treatment duration. The untreated specimen had an average CA of 47.5°, indicating moderate wettability (Fig. 11(a2)). Electrochemical treatment significantly reduced the CA, and the reduction rate slowed with prolonged treatment (Fig. 11(b2) and (c2)). The average CA decreased to 6.6° at 270 s and reached a minimum of 6.3° at 180 s (Fig. 11(l2)). These results confirm the effectiveness of electrochemical treatment in enhancing the wettability of aluminum alloy surfaces.

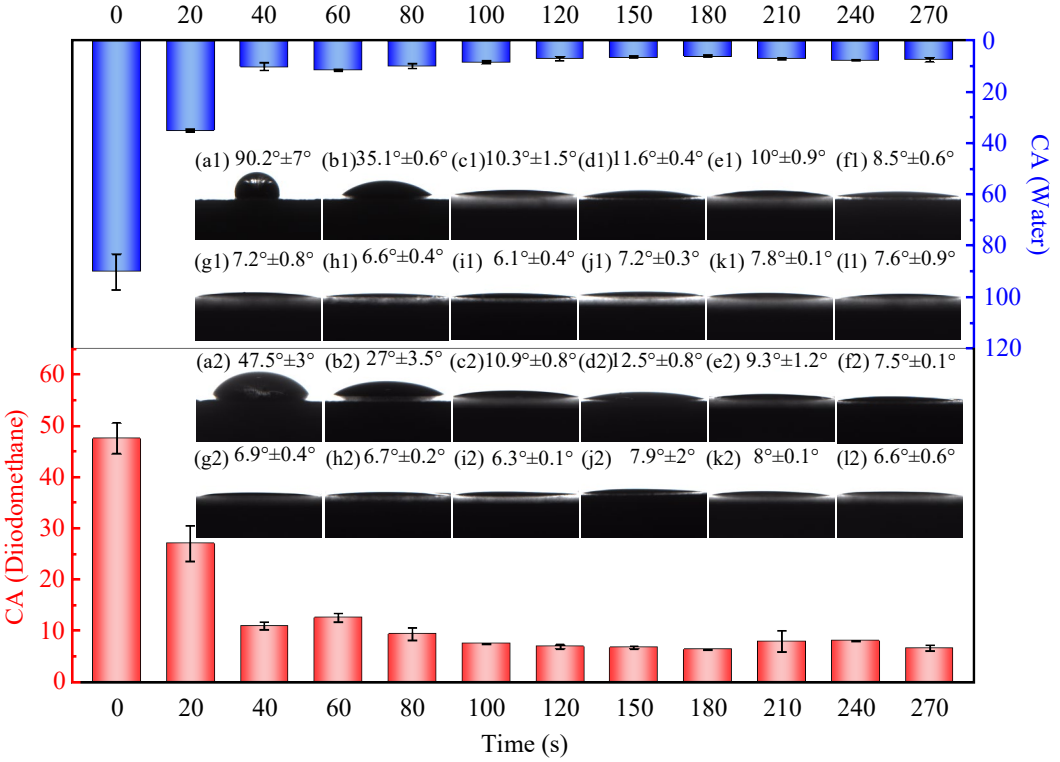

Fig. 11. CA of (a1) - (l1) water and (a2) - (l2) diiodomethane on the surface of the specimens under different treatment times, (a) - (l) corresponding to treatment times of 0 - 270 s, respectively.

The SFE (γ_s) and its components (γ_s^D and γ_s^P) of aluminum alloy specimens were determined at different treatment durations, as shown in Table 7. Results show that, after 20 s of treatment, γ_s^D increased from 35.656 to 45.413 mJ/m², and γ_s^P increased from 1.381 to 23.631 mJ/m², indicating that electrochemical treatment effectively improves surface hydrophilicity and chemical activity. This enhancement is expected to increase the contact area and adhesion between the substrate and adhesive. SFE

values continued to rise with prolonged treatment, further improving surface properties, and stabilized after 80 s.

The CA and SFE experiments demonstrate that treatment duration significantly affects the wettability and SFE of aluminum alloys. SFE and hydrophilicity increased initially with treatment time and stabilized after 80 s. Notably, excessively long treatment durations had minimal impact on surface properties while continuing to reduce surface roughness. Therefore, the comprehensive effects of electrochemical treatment duration on the surface morphology and wettability of aluminum alloy specimens should be considered simultaneously in practical applications to achieve the optimal bonding properties.

Table 7

The OWRK method is used to derive γ_S^D, γ_S^P, and γ_S (mJ/m^2) values for aluminum alloy specimens at different treatment times.

Treatment durations	γ_S^D	γ_S^P	γ_S
As-received	35.656	1.381	37.037
20 s	45.413	23.631	69.045
40 s	49.887	30.184	80.072
60 s	49.602	30.088	79.691
80 s	50.134	30.11	80.245
100 s	50.366	30.229	80.595
120 s	50.432	30.369	80.802
150 s	50.453	30.429	80.883
180 s	50.493	30.463	80.957
210 s	50.319	30.427	80.746
240 s	50.306	30.356	80.663
270 s	50.463	30.303	80.766

Fig. 12 shows the average shear strength of SLJs after various treatment durations. The average shear strength increased initially with treatment duration, then decreased slightly, and eventually stabilized. Compared to untreated joints, the average strength increased by 55% to 6.43 MPa and 75% to 7.26 MPa after 20 s and 40 s of treatment, respectively. At 60 s and 80 s, the strength further increased to 9.35 MPa and 9.41 MPa, respectively. The maximum strength was achieved at 100 s, representing a 170% improvement over untreated joints. As shown in Fig. 10 and Table 7, this significant

enhancement is attributed to the synergistic effects of increased surface roughness Sa and surface free energy SFE, which improve interface compatibility between the adhesive and substrate. However, a slight reduction in strength was observed when treatment duration exceeded 100 s. At 120 s, the strength decreased to 9.27 MPa, approximately 17% lower than that at 100 s. From 180 s to 270 s, the strength stabilized at approximately 8.5 MPa. This phenomenon is attributed to the reduction and stabilization of the S_a values and the surface chemical state during treatment.

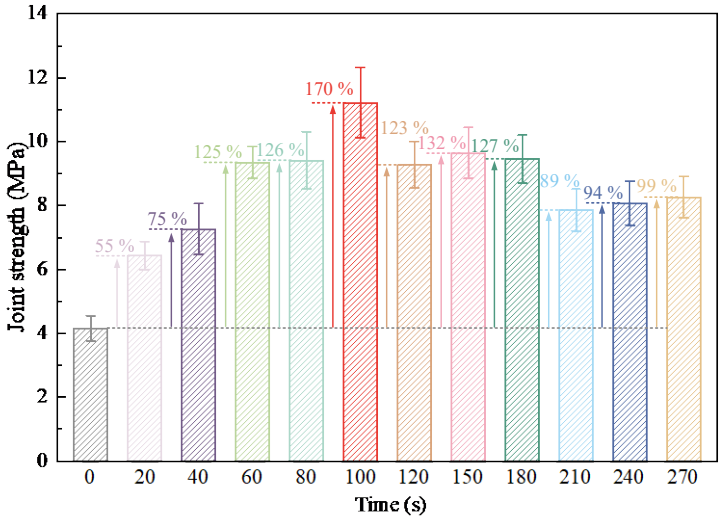

Fig. 12. The average shear strength of SLJs at different treatment times.

3.3 Comparison of surface properties and joint strength with various pre-treatments

This section compares the surface properties and bond strength of aluminum alloy specimens subjected to mechanical grinding, sandblasting, and electrochemical treatment. The electrochemical treatment was performed at a current density of 0.8 $A \cdot cm^{-2}$ for 100 s. To ensure comparability, the surface roughness S_a of the mechanically ground and sandblasted specimens was adjusted to approximately 4 μm, similar to that of the electrochemically treated specimens. The specimens are designated as Model-1 (untreated), Model-2 (ground), Model-3 (sandblasted), and Model-4 (electrochemically treated).

Fig. 13 illustrates the surface morphology and roughness S_a of aluminum alloy specimens under different pre-treatment methods, where panels (a) to (d) correspond to Models 1 to 4, respectively. Subpanels (a1)-(d1) display industrial camera (IC) images, (a2)-(d2) show SEM images revealing 2D morphology, and (a3)-(d3) present WLI

images showing 3D morphology. As shown in Figs. 13(a1)-(a3) and (b1)-(b3), Model-1 and Model-2 surfaces exhibit characteristic grinding scratches with average S_a values of 2.88 μm and 4.04 μm, respectively. In contrast, Model-3 has a relatively homogeneous surface with micro-craters and an average S_a of 3.93 μm. Model-4 shows a more uniform morphology with an average S_a of 4.044 μm.

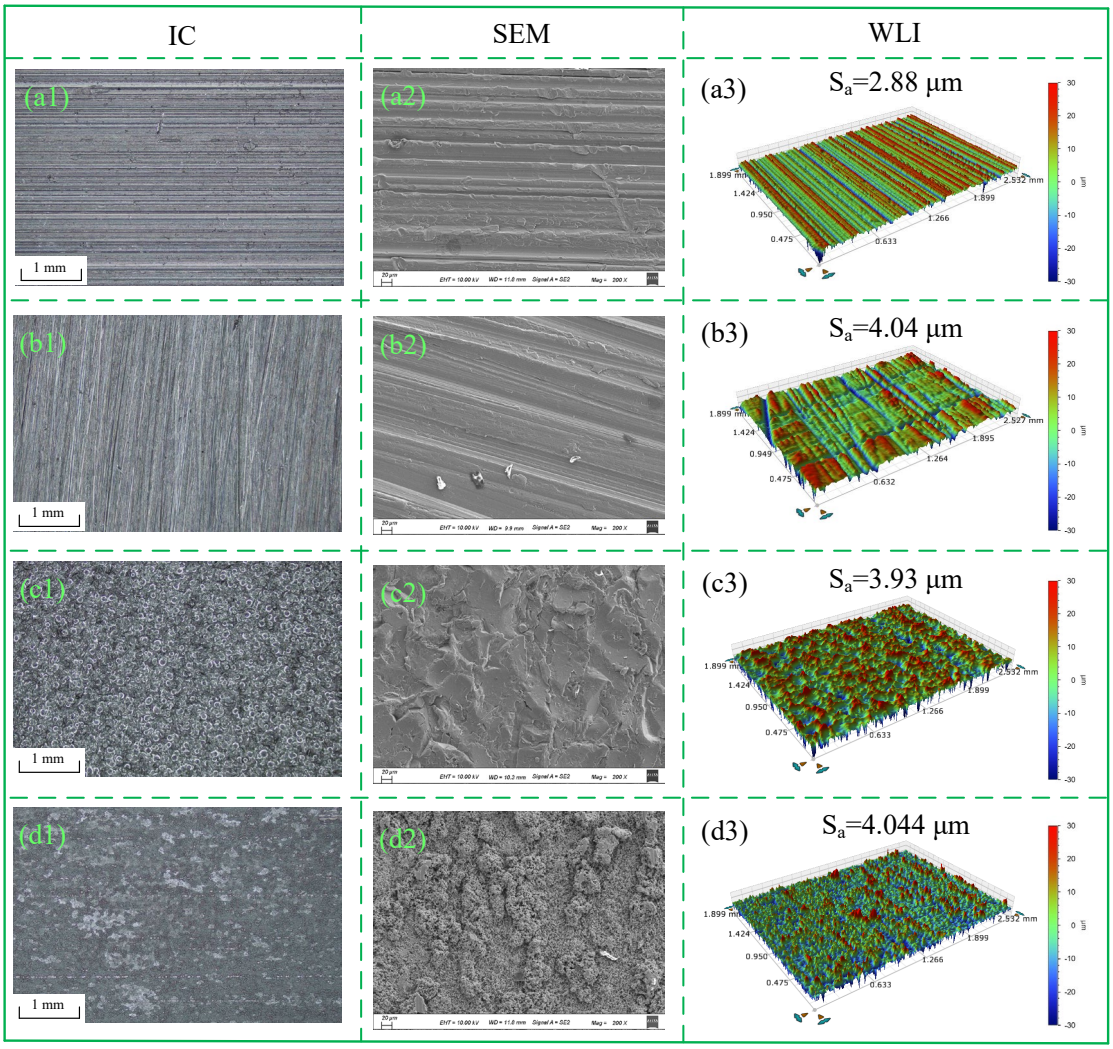

Fig. 13. Comparison of surface morphology of aluminum alloy specimens under different pre-treatment conditions: IC, SEM, WLI, (a)-(d) correspond to Models 1-4, respectively.

Fig. 14 and Table 8 present the CA and SFE measurements for the aluminum alloy surfaces under different treatments. The CA values for water and diiodomethane on Model-1 are 90.2° and 47.5°, respectively (Figs. 14(a) and (e)). Model-2 shows a slight decrease in SFE compared to Model-1, which may be due to the increased S_a from grinding, leading to a more hydrophobic surface [58]. In contrast, Model 3 exhibits a slight increase in hydrophilicity and SFE relative to Models 1 and 2, indicating that

sandblasting improves surface chemical properties more effectively than grinding. Notably, Model-4 has significantly lower CAs for water and diiodomethane, corresponding to 8.5° and 7.5°, respectively, compared to other models (Figs. 14(d) and (h)). Concurrently, Model-4 demonstrates high SFE values: 80.595 mJ/m² for the total SFE, 50.366 mJ/m² for the polar component, and 30.229 mJ/m² for the dispersive component. This rise suggests that electrochemical treatment simultaneously modifies S_a and enhances hydrophilicity and SFE. The increase in the polar component confirms that electrochemical treatment alters the surface chemical state.

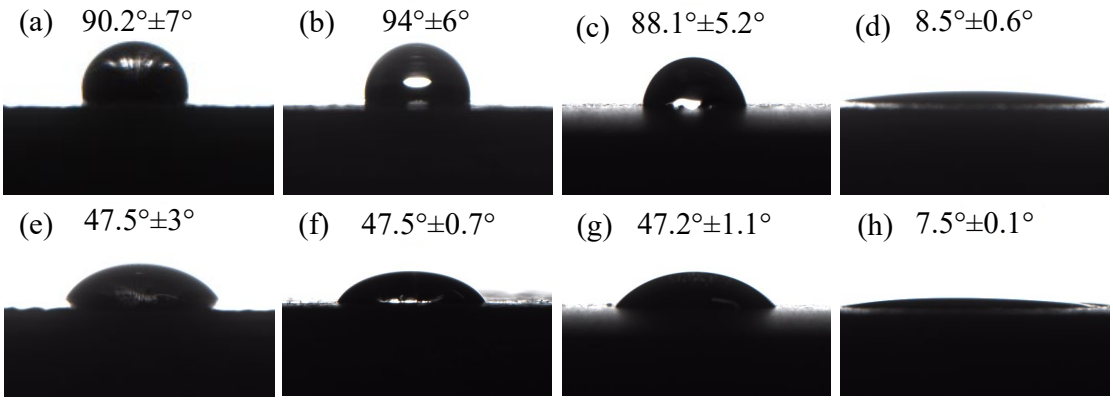

Fig. 14. The CA of (a)-(d) water, (e)-(f) diiodomethane on (a) and (e) Model-1, (b) and (f) Model-2, (c) and (g) Model-3, (d) and (h) Model-4.

Table 8

γ_S^D, γ_S^P and γ_S (mJ/m^2) values for aluminum alloy specimens under different pre-treatments.

Treatment methods	γ_S^D	γ_S^P	γ_S
Model-1	35.656	1.381	37.037
Model-2	35.657	0.701	36.358
Model-3	35.820	1.83	37.651
Model-4	50.366	30.229	80.595

Fig. 15 shows the cross-sectional morphology of adhesive joints for the four treatment methods. The adhesive layer maintains consistent thickness across all samples, with no macroscopic debonding or voids at the interface, indicating satisfactory initial adhesion for each pre-treatment method [24]. Previous studies highlight the need for auxiliary processes, such as resin pre-coating, to optimize adhesion by ensuring wettability and complete bonding [59,60]. However, in this study, micro-cavities are seamlessly filled with adhesive, particularly in Model-4, which has

the most complex morphology due to electrochemical corrosion-induced micro-pits. This is attributed to the enhanced hydrophilicity from electrochemical treatment (Fig. 14).

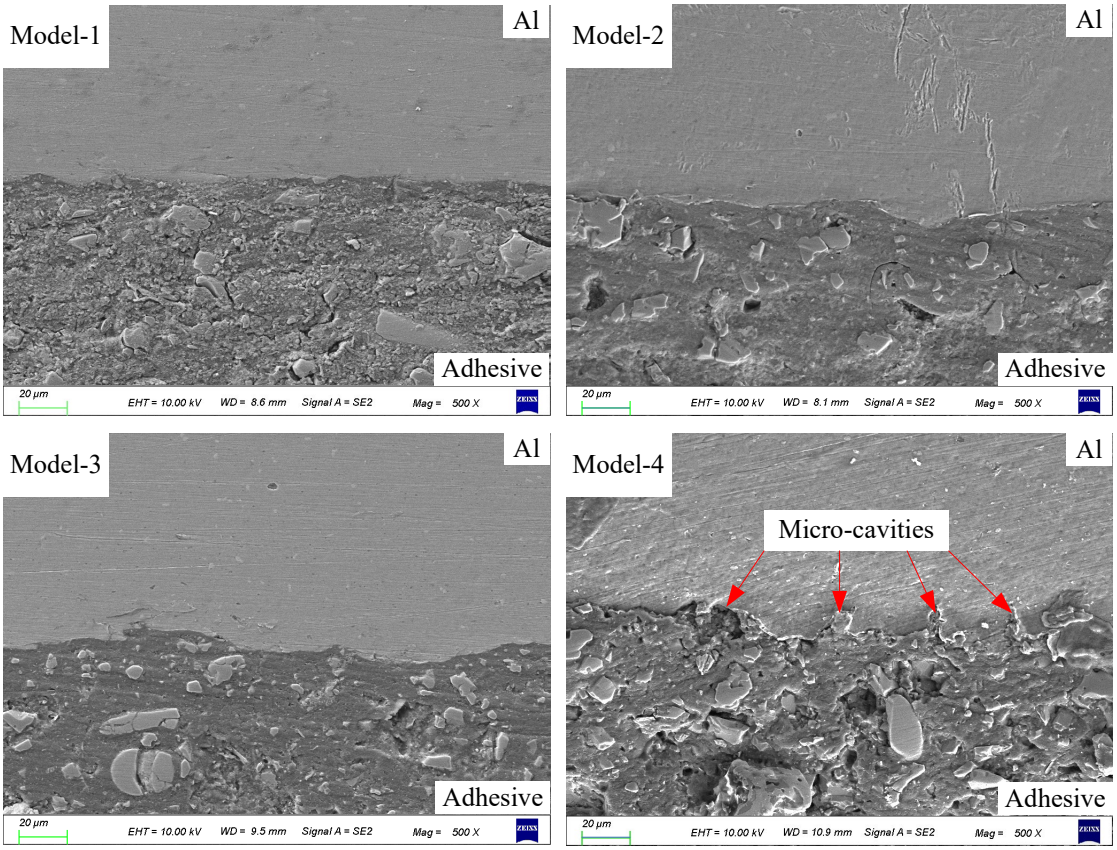

Fig.15. Cross-sectional morphology of the adhesive joint under four surface treatments

Fig. 16 presents the SLJ test results for different pre-treatments, where Fig. 16(a) shows the average shear strength, and Fig. 16(b) displays representative load-displacement curves. The average shear strength of Model-2 joints increases by approximately 22% compared to Model-1, due to the higher S_a improving mechanical interlocking. Model-3 joints show a 58% increase in strength relative to Model-1, attributed to enhanced SFE promoting better adhesion. Notably, Model-4 joints achieve the highest average bond strength and maximum load, corresponding to 11.22 MPa and 7014 N, respectively, representing a 170% improvement over Model-1. Additionally, Model-4 exhibits the most considerable plastic deformation before failure, as indicated by the most significant area under the curve in Fig. 16(b).

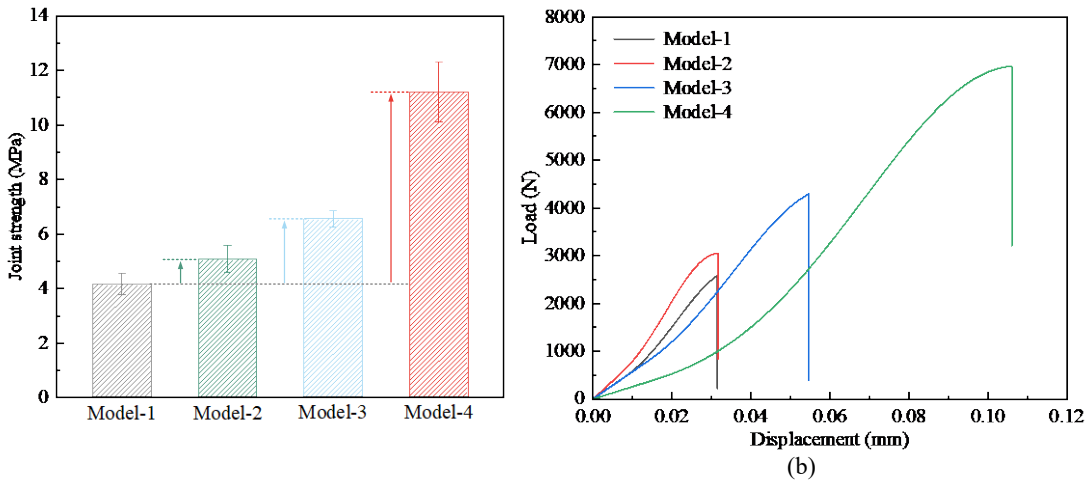

Fig. 16. SLJs test results, (a) average shear strength of various SLJs, and (b) representative load-displacement curves.

Fig. 17 displays the fracture surfaces and SEM images of joint failures for the four models. The adhesive layer is shown on the left (Figs. 17(e)-(h)), and the metal substrate on the right (Figs. 17(i)-(l)). The results indicated that regarding Models 1 to 3, the fracture surfaces were almost entirely covered by adhesive on the left side (Figs. 17(e)-(g)), while the right side retained only a small amount of adhesive, exposing the substrate surface (Figs. 17(e)-(g)). This observation aligns with the standard interface failure mechanism illustrated in Fig. 4(b). The variation in residual adhesive among the three models can be attributed to differences in S_a and SFE. For instance, minimal residual adhesive was observed on the Model-1 substrate (Fig. 17(i)). In contrast, Model-2 retained more adhesion due to enhanced mechanical interlocking from increased surface roughness. Furthermore, Model-3 exhibited a more pronounced residual adhesive layer with a torn morphology compared to Model-2. This phenomenon may be ascribed to increased surface roughness and hydrophilicity (Fig.14). In comparison, Model-4 joints exhibited a shift from interface to mixed failure mode (Fig. 17(d)), suggesting significantly enhanced adhesive strength at the interface. This provides substantial evidence for the considerable strength increase shown in Fig. 16. Notably, the S_a value of Model-4 is comparable to those of Models 2 and 3 (Fig. 13), yet the shear strength of Model-4 joints was approximately double, with distinct fracture modes. Therefore, besides mechanical interlocking from electrochemical

treatment, changes in surface chemical state, such as specific active groups, may also contribute to the strength increase and fracture mode shift [52].

In conclusion, the surface roughness and adhesion strength of aluminum initially increase and then decrease with varying current densities and treatment durations. This trend can be primarily attributed to the mechanical interlocking effect stemming from enhanced surface roughness. Notably, while the surface roughness values for Model-2 and Model-4 are similar (4.04 and 4.044 μm, respectively), the improvement in joint strength is 22% and 170%, respectively. This disparity can be attributed to variations in surface wettability and the distinct textures achieved through different surface treatment methods. Interestingly, samples electrochemically treated for 40 s and 100 s present analogous surface roughness and wettability values, yet the enhancement in joint strength is 75% and 170%, respectively. The minor difference in surface texture observed in Fig. 9(c) and (g) alone cannot account for an increase of up to 95% in the bonding strength. Hirchenhahn et al found that the chemical bond that determined the interfacial reliability of the hybrid would be formed between oxygen within the thermoplastic and aluminum within the surficial oxide layer of the aluminum alloy, during the welding process [61]. Therefore, based on the presented results and existing literature, it is posited that chemical bonding may also play a pivotal role in the properties of electrochemically treated specimens [3,24].

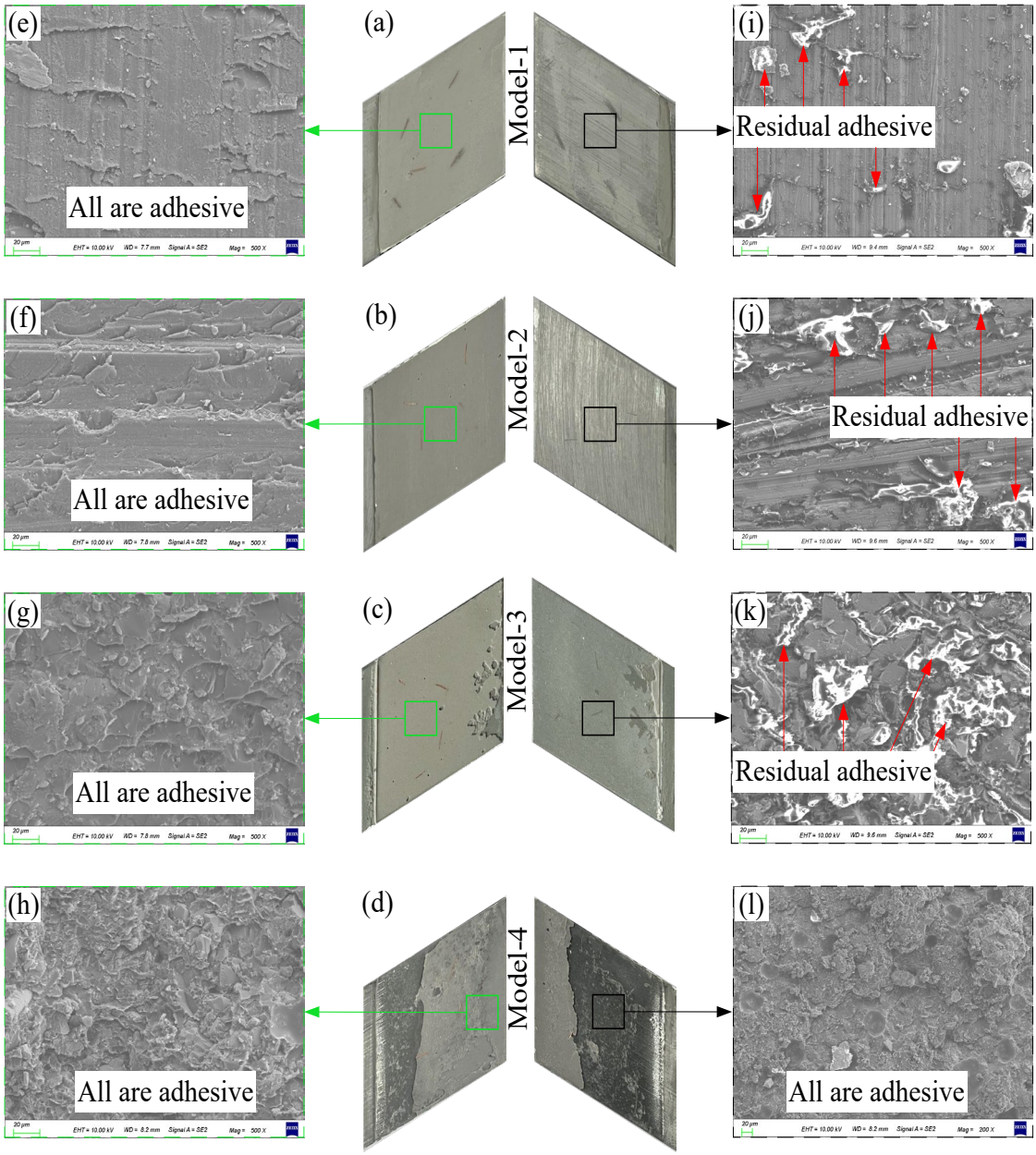

Fig. 17. Photographs and SEM images of fracture surfaces of different pre-treatments, (a)-(d) photographs of fracture surfaces for Models 1-4 joints, (e)-(h) SEM images of adhesive side, and (i)-(l) SEM images of metal side.

4. Surface Chemistry Evolution and Adhesion Mechanism

4.1 XPS characterization and surface atomic composition

The XPS spectra of aluminum alloy specimens and the atomic content of major elements under different pre-treatments are shown in Fig. 18. All pre-treated surfaces contain C, O, N, and Al. In contrast, Na and Cl elements appear only on the electrochemically pre-treated surface. Relative to the as-received surface Model-1, the C content decreases for all treated specimens, with the most significant drop for Model-4 from 67.38% to 31.31%. In parallel, both O and Al increase, most prominently in

Model-4, from 22.39% to 42.23% for O and from 5.04% to 14.46% for Al. This phenomenon indicates effective removal of organic contaminants and concurrent formation of a denser oxide layer [62].

The electrochemical treatment drives a dissolution-repassivation cycle. Initially, the native contaminants and thin oxide layer are removed under the external potential. Subsequently, a new AlOOH/Al_2O_3-enriched layer is rapidly rebuilt under NaCl neutral media. Cl^- in the electrolyte promotes localized dissolution with pit-like initiation, while external potential facilitates rapid repassivation, forming a denser surface layer with fewer defects and a higher density of hydroxyl sites [63]. The detection of trace Na^+ and Cl^- is primarily due to adsorption on the surface rather than deep penetration. In contrast, mechanical methods only produce physical decontamination and transient exposure of fresh Al metal. The subsequently formed native film is thin and has a limited density of hydroxyl sites, resulting in a weaker decrease in C and an increase in O and Al compared to the electrochemical method.

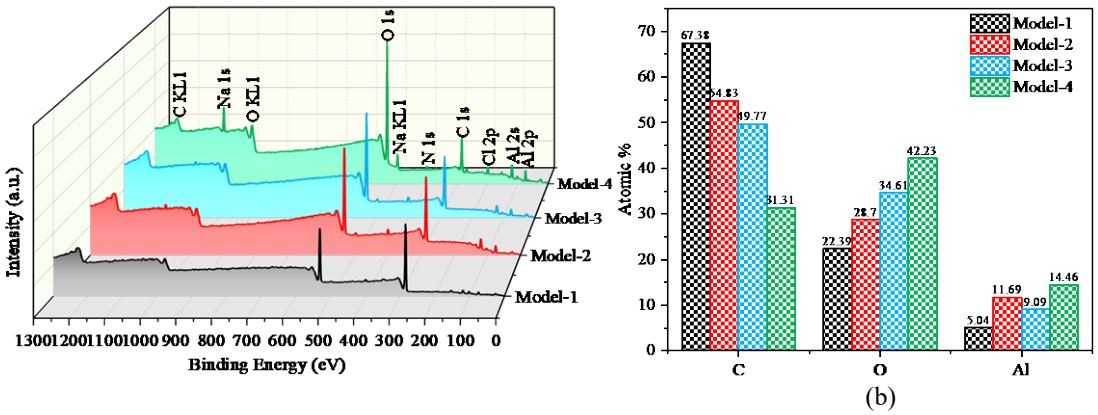

Fig. 18. XPS spectra and corresponding atomic content of elements of the aluminum alloy surface for the four Models, (a) Survey spectra and (b) atomic content of elements.

As shown in Fig. 19, the high-resolution narrow-scan XPS spectra of C 1s (a-d), Al 2p (e-h), and O 1s (i-l) were obtained from the substrate surface after different pre-treatments. The C 1s spectrum reveals a diminished C-C(H) component across all treated surfaces, with Model-4 demonstrating the most significant reduction. It confirms the effective removal of adventitious organic pollutants via anodic dissolution and surface renewal [52]. The electrochemical treatment eliminates surface organic pollutants and weakly attached organic matter through electrochemical dissolution and

bubble microflow shear. The subsequently formed hydroxylated oxide layer has a lower tendency to re-adsorb non-polar pollutants. In contrast, grinding and sandblasting may adsorb organic pollution by introducing mechanical grit and a cold-work hardening layer, leading to higher C-C(H) residues.

High-resolution XPS spectra of Al 2p on aluminum alloy surfaces subjected to different pre-treatments revealed a significant increase in alumina and aluminum hydroxide content in Models 2-4 compared to Model 1 (Figs. 19(e)-(h)). Notably, the metallic Al content was higher on ground specimens than on other treatments, due to over-processing during grinding that exposed the aluminum matrix (Fig. 13(b2)). Regarding O 1s spectra, electrochemical treatment resulted in a notable increase in aluminum hydroxide content. This is attributed to the gradual dissolution of aluminum ions during electrochemical processing, which, in the presence of hydroxide ions from the electrolyte, formed an adherent aluminum hydroxide layer. This layer exhibited high hydrophilicity, enhancing adsorption and binding capacity compared to aluminum oxide, thereby increasing the SFE [64]. These findings corroborate the improved bond strength of electrochemically treated joints (Fig. 16). Additionally, both sandblasting and electrochemical treatments enhanced metal oxides relative to the untreated surface. Sandblasting may densify the oxide layer through extrusion of the existing oxide layer, while electrochemical treatment promotes oxide and hydroxide formation on the anode. Aluminum hydroxide can transform into more stable aluminum oxide, sustaining high surface oxygen content. These newly formed aluminum hydroxide and oxide layers may react chemically with the adhesive, thereby enhancing the adhesive strength of the colloid to the substrate surface [24,65].

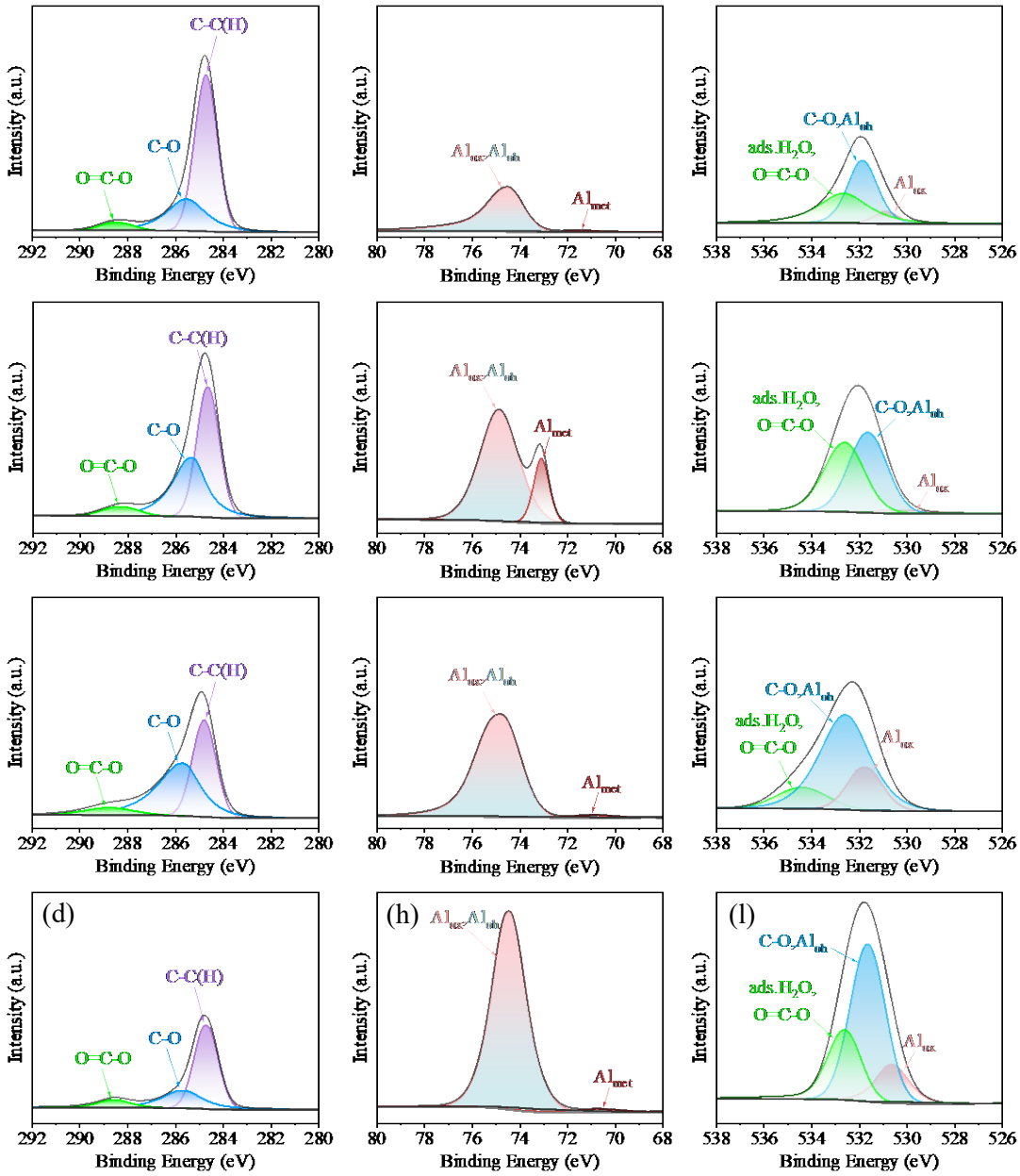

Fig. 19. High-resolution spectra of (a-d) C 1s, (e-h) Al 2p and (i-l) O 1s for (a, e, i) Model-1, (b, f, j) Model-2, (c, g, k) Model-3 and (d, h, l) Model-4 etched under different pretreatment conditions

4.2 FTIR characterization and adhesion enhancement mechanism

FTIR analysis was introduced to evaluate the impact of varying surface pre-treatments on the surface chemical functional groups, as shown in Fig. 20(a) and Table 9. Regarding the electrochemical treatment Model-4, the O-H stretching band shows blue shifts from 3302.52 to 3331.41 cm^{-1}, with increased intensity compared to the as-received specimens Model-1. This shift reflects the enhancement of the free hydroxyl group density due to AlOOH formation and the weakening of hydrogen bonds [66]. Meanwhile, the symmetric C-H stretching moves from 2851.40 to 2868.57 cm^{-1},

whereas the asymmetric C-H stretching exhibits a slight red shift from 2921.89 to 2914.41 cm^{-1}, indicating reduced long-chain organic pollutants [65]. Furthermore, the invariability of v(C=C), δ(C-H), and v(C-O-C_s) peaks verifies aromatic backbone stability.

Table 9
FTIR results of adhesive joint interfaces under different pre-treatments.

	Model-1	Model-2	Model-3	Model-4
v(O-H)	3302.52	3297.82	3301.79	3331.41
$v(C\text{-}H)_{as}$	2921.89	2922.52	2921.91	2914.41
$v(C\text{-}H)_s$	2851.40	2850.92	2850.42	2868.57
v(C=C)	1608.26	1608.71	1608.86	1608.29
	1509.14	1509.39	1509.16	1509.56
δ(C-H)	1452.35	1452.57	1452.46	1452.81
$v(C\text{-}O\text{-}C_s)$	1243.37	1244.40	1243.88	1244.76
	1036.97	1038.06	1038.49	1037.76

The excellent bonding performance of the electrochemically treated joints is related to the synergistic effect of mechanical interlocking and chemical bonding, which the traditional mechanical pre-treatment cannot achieve. Grinding and sandblasting only enhance the mechanical anchorage by increasing the surface roughness. However, they have little effect on the modification of surface chemistry, as shown in the XPS spectra (Fig. 19), where the organic contamination still exists and no reactive hydroxide layer is formed on the surface. On the contrary, electrochemical treatment realizes the physical and chemical modifications simultaneously. It produces the micro-pitted morphology (Figs. 5, 6, 9, 10) for mechanical interlocking and generates a hydroxyl-rich aluminum hydroxide layer (Fig. 19(h), (l)) on the surface. The hydroxyl groups on the surface can interact with the epoxy adhesive at the molecular level.

The predominant chemical reinforcement mechanism is proposed to be the formation of robust Al-O-C covalent bonds, facilitated through a hydroxyl-induced epoxy ring-opening reaction, as shown in Fig. 20(b). This proposition is bolstered by multiple converging lines of evidence: a significant escalation in hydroxyl content as demonstrated by XPS (Fig. 19(l)), a marked shift in the O-H stretching vibration as shown in FTIR spectra (Fig. 20(a), Table 9), and a transition in failure mode from interfacial to cohesive/mixed (Fig. 17). While hydrogen bonding might play a role in

initial adhesive wetting, its comparatively low binding energy relegates it to a secondary factor behind the stable, cross-linked network engendered by covalent bonds [67]. The substantial 170% improvement in strength is partially due to the chemical bonding mechanism, which is absent in purely mechanical treatments and difficult to achieve through surface roughness, microscopic morphologies, and wettability alone.

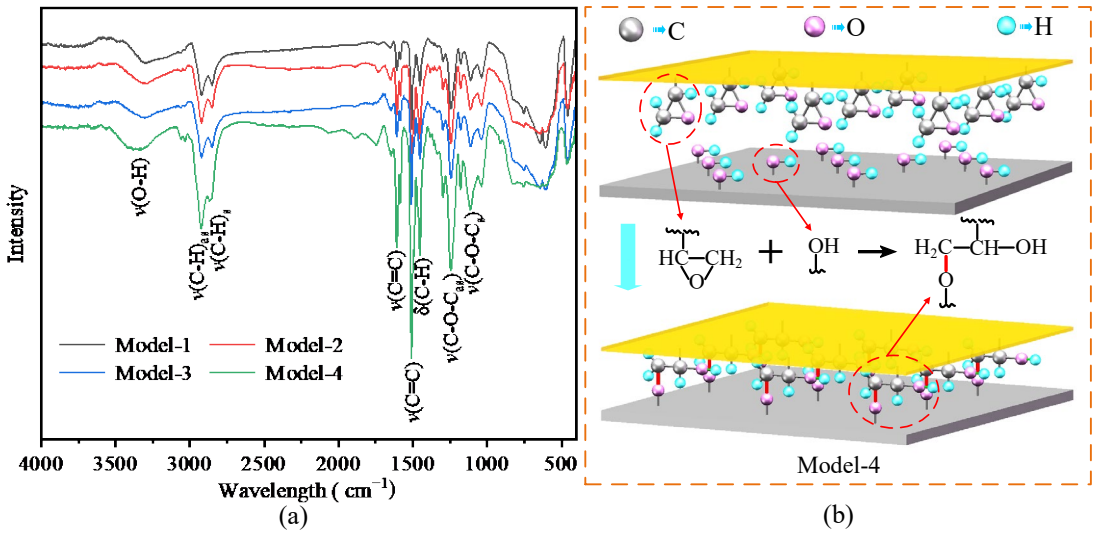

Fig. 20. FTIR spectra of the adhesive joint interface for the four Models and the major covalent bonds forming process at the substrate-adhesive interface after electrolytic treatment, (a) FTIR spectra, (b) the major covalent bonds forming process.

This mechanistic understanding is consistent with and complements previous research. The critical role of surface hydroxyl groups in interfacial covalent bonding is well-established in plasma treatment studies [65,66], and synergistic physico-chemical enhancement has been documented [26,36]. However, as demonstrated here, electrochemical treatment in a neutral salt solution not only replicates this robust mechanism but also offers distinct advantages. Specifically, it achieves a superior strength increase of 170%, compared to laser texturing (107%) or nanofiber interleaving (145%) [5,6]. Furthermore, this method is more environmentally friendly and industrially scalable than anodizing or aggressive chemical etching. Thus, electrochemical pre-treatment enables a highly effective and sustainable approach for high-performance adhesive bonding of aluminum alloys.

5. Conclusion

This study investigated the electrochemical treatment of aluminum alloys in neutral salt solutions. Results revealed the influence of electrochemical parameters on

the surface characteristics and adhesive properties of the alloys. By combining multiple characterization methods, the interface-strengthening mechanisms of electrochemical and traditional mechanical treatments were compared, highlighting the critical role of chemical bonding in enhancing interface strength. The main conclusions are outlined as follows:

(1) Current density significantly regulates the surface properties of aluminum alloys. At a current density of 0.8 A cm^{-2}, the surface roughness S_a increased from 2.88 μm to 4.088 μm, and the contact angle CA of water droplets decreased from 90.2° to 11.6°, leading to a 125% increase in shear strength compared to untreated joints.

(2) Processing duration exhibited time-dependent effects on surface properties. At 100 s of processing duration, S_a reached 4.044 μm, and CA decreased to 8.5°. The shear strength increased by approximately 170% due to the combined effects of surface morphology and wettability.

(3) XPS and FTIR results showed that electrochemical treatment significantly increased the hydroxyl (-OH) content on the alloy surface. These hydroxyl groups underwent ring-opening reactions with epoxy resin groups, forming chemical bonds. This mechanism promoted a transition from interface failure to mixed failure in the joints.

(4) Under identical roughness conditions, the shear strength of electrochemically treated joints was 120% higher than that of mechanically treated joints. This improvement is attributed to two mechanisms: mechanical interlocking from more complicated surface morphology and improved wettability, and chemical strengthening from surface functional groups.

This work systematically elucidated the mechanisms and principles of enhancing the bonding properties of thin-walled aluminum alloys via electrochemical pre-treatment in neutral salt solutions. Multi-scale characterization techniques confirmed the crucial role of chemical bonding in interface strength. However, uneven current density distribution remains a major challenge, limiting the application to large or complex-shaped components. Future research could focus on optimizing irregular electrode designs, developing strategies for current density uniformity, and creating

programmable, efficient, and automated electrochemical treatment equipment for industrial applications.

Author Statement

We declare that this manuscript, entitled "Electrochemical pre-treatment of aluminum alloy in environmentally friendly medium: Parameter optimization and bonding strengthening mechanism," is original, has not been published before, and is not currently being considered for any publication elsewhere.

We confirm that the manuscript has been read and approved by all named authors and that there are no other persons who satisfied the criteria for authorship but are not listed. We further confirm that the order of authors listed in the manuscript has been approved by all of us.

We understand that the Corresponding Author is the sole contact for the Editorial process. He is responsible for communicating with the other authors about progress, submissions of revisions, and final approval of proofs.

CRediT authorship contribution statement

Qifan Hu: Writing–original draft, Data processing. **Zhenghui Ge:** Writing–review & editing, Methodology, Funding acquisition. **Kai Pang:** Writing–review & editing, Data processing. **Yongwei Zhu:** Supervision, Funding acquisition. **Xiaonan Hou:** Writing–review & editing, Supervision.

Declaration of competing interest

The authors declare that they have no known competing financial interests or personal relationships that could have appeared to influence the work reported in this paper.

Acknowledgments

This work was financially supported by the Insight Action Project of China (3ED537F8), and the National Natural Science Foundation of China (52175438).

Data availability

Data will be made available on request.

References

[1] X. You, Z. Xing, S. Jiang, Y. Zhu, Y. Lin, H. Qiu, R. Nie, J. Yang, D. Hui, W. Chen, Y. Chen, A review of research on aluminum alloy materials in structural engineering, Dev. Bui. Environ. 17 (2024) 100319, https://doi.org/10.1016/j.dibe.2023.100319.

[2] L. Duan, W. Liang, Y. Hou, D. Wang, J. Cui, G. Li, H. Jiang, Investigation on shear and fatigue

performance of CFRP/aluminum alloy single-lap adhesive joint, Thin. Wall. Struct. 196 (2024) 111421, https://doi.org/10.1016/j.tws.2023.111421.

[3] X. Bi, Z. Luo, B. Liu, M. Xu, Z. Wang, Enhancing interfacial reliability of metal–thermoplastic hybrid joints via adding carbon fiber and adjusting welding heat input, ACS Appl. Mater. Interfaces 13(28) (2021) 33722-33733, https://doi.org/10.1021/acsami.1c08977.

[4] B. Zhang, Y. Ma, F. Yu, Y. Liu, E. Zhou, Z. Fan, E. Ge, Y. Li, Z. Lin, Strengthening flat-die friction self-pierce riveting joints via manipulating stir zone geometry by tailored rivet structures, Int. J. Mach. Tool. Manu. 203 (2024) 104223, https://doi.org/10.1016/j.ijmachtools.2024.104223.

[5] F. Zhu, L. Ke, Z. Feng, J. Zhou, C. Li, R. Zhang, Enhancing bond performance of CFRP-steel epoxy-bonded interface by electrospun nanofiber veils, Thin. Wall. Struct. 198 (2024) 111765, https://doi.org/10.1016/j.tws.2024.111765.

[6] H. Wan, J. Min, J. Lin, B. Carlson, S. Maddela, C. Sun, Effect of laser spot overlap ratio on surface characteristics and adhesive bonding strength of an Al alloy processed by nanosecond pulsed laser, J. Manuf. Process. 62 (2021) 555-565, https://doi.org/10.1016/j.jmapro.2020.12.055.

[7] Y. Wei, G. Zheng, Q. Luo, Q. Li, G. Sun, On impact response and damage tolerance of adhesively bonded joints–An experimental and numerical study, Thin. Wall. Struct. 208 (2025) 112606, https://doi.org/10.1016/J.TWS.2024.112606.

[8] T.H. Loutas, P.M. Kliafa, G. Sotiriadis, V. Kostopoulos, Investigation of the effect of green laser pre-treatment of aluminum alloys through a design-of-experiments approach, Surf. Coat. Tech. 375 (2019) 370-382, https://doi.org/10.1016/j.surfcoat.2019.07.044.

[9] N. Saleema, D.K. Sarkar, R.W. Paynter, D. Gallant, M. Eskandarian, A simple surface treatment and characterization of AA 6061 aluminum alloy surface for adhesive bonding applications, Appl. Surf. Sci. 261 (2012) 742-748, https://doi.org/10.1016/j.apsusc.2012.08.091.

[10] R. Zheng, J. Lin, P. Wang, C. Zhu, Y. Wu, Effect of adhesive characteristics on static strength of adhesive-bonded aluminum alloys, Int. J. Adhes. Adhes. 57 (2015) 85-94, https://doi.org/10.1016/j.ijadhadh.2014.10.007.

[11] H. Wang, C. Zhang, Y. Chen, Z. Liu, Y. Wang, L. Hua, Study on adhesive-film bonded Al/CFRP joints strengthened by ultrasonic vibration, Thin. Wall. Struct. 191 (2023) 111072, https://doi.org/10.1016/j.tws.2023.111072.

[12] P. Soranansri, A. Dubois, P. Moreau, T. Funazuka, K. Dohda, L. Dubar, Initial and grow-up stages of material transfer on Arc-DLC coating in aluminum forming processes at high temperatures, Wear 556 (2024) 205491, https://doi.org/10.1016/j.wear.2024.205491.

[13] D.W. Seo, H.C. Yoon, J.Y. Lee, J.K. Lim, Effects of surface treatment and loading speed on adhesive strength of aluminum to polycarbonate lap joints, Key Eng. Mater. 261 (2004) 405-410, https://doi.org/10.4028/www.scientific.net/KEM.261-263.405.

[14] Z. Feng, H. Zhao, C. Tan, X. Zhang, B. Chen, X. Song, Nanosecond laser ablation for improving the strength of CFRTP and aluminum alloy adhesively bonded joints, Compos. Struct. 274 (2021) 114369, https://doi.org/10.1016/j.compstruct.2021.114369.

[15] M.R.P. Pavlović, S.G. Eraković, M.M. Pavlović, J.S. Stevanović, V.V. Panić, N.L. Ignjatović, Anaphoretical/oxidative approach to the in-situ synthesis of adherent hydroxyapatite/titanium oxide composite coatings on titanium, Surf. Coat. Tech. 358 (2019) 688-694, https://doi.org/10.1016/j.surfcoat.2018.12.003.

[16] S.T.D. Freitas, M.D. Banea, S. Budhe, S.D. Barros, Interface adhesion assessment of composite-to-metal bonded joints under salt spray conditions using peel tests, Compos. Struct. 164 (2017) 68-75, https://doi.org/10.1016/j.compstruct.2016.12.058.

[17] F.P. Hu, J. Qin, Q.W. Zeng, F. Wang, X. Zhang, N.Y. Zhang, S.Z. Wang, P. Huang, Z.H. Fan, X.D. Peng, W.D. Xie, Research on surface treatment of magnesium alloy and its wettability with resin, Mater. Sci. Tech. 32(10) (2016) 963-968, https://doi.org/10.1080/02670836.2015.1104020.

[18] M. Chandrasekar, M.R. Ishak, M.S. Salit, Z. Leman, M. Jawaid, J. Naveen, Mechanical properties of a novel fibre metal laminate reinforced with the carbon, flax, and sugar palm fibres, BioResources 13(3) (2018) 5725-5739, https://doi.org/10.15376/biores.13.3.5725-5739.

[19] J. Li, Y. Li, M. Huang, Y. Xiang, Y. Liao, Improvement of aluminum lithium alloy adhesion performance based on sandblasting techniques, Int. J. Adhes. Adhes. 84 (2018) 307-316, https://doi.org/10.1016/j.ijadhadh.2018.04.007.

[20] J.V. Dam, S.T. Abrahami, A. Yilmaz, Y. Gonzalez-Garcia, H. Terryn, J.M.C. Mol, Effect of surface roughness and chemistry on the adhesion and durability of a steel-epoxy adhesive interface, Int. J. Adhes. Adhes. 96 (2020) 102450, https://doi.org/10.1016/j.ijadhadh.2019.102450.

[21] S. Jiang, A. Zhang, X. Zhan, H. Jiang, Surface microtexturing design, laser-etching and adhesive failure of aluminum alloy single-lap-joint: Experiment and simulation, Thin. Wall. Struct. 193 (2023) 111237, https://doi.org/10.1016/j.tws.2023.111237.

[22] D. Mamalis, W. Obande, V. Koutsos, J.R. Blackford, C.M.O. Brádaigh, D. Ray, Novel thermoplastic fibre-metal laminates manufactured by vacuum resin infusion: the effect of surface treatments on interfacial bonding, Mater. Design 162 (2019) 331-344, https://doi.org/10.1016/j.matdes.2018.11.048.

[23] Y. Shin, Y. Qiao, N. Canfield, Z. Yu, H.M. Meyer, D.R. Merkel, E.K. Nickerson, N.S. Kanbargi, A. Ortiz, A.K. Naskar, K.L. Simmons, Significant slowdown of plasma-optimized surface energy deactivation by vacuum sealing for efficient adhesive bonding, Compos. Part. B-Eng. 240 (2022) 110001, https://doi.org/10.1016/j.compositesb.2022.110001.

[24] X. Bi, Z. Wang, M. Xu, X. Li, Femtosecond laser fabricated micro/nano interfacial structures to strengthen CFRPEEK/A6061-T6 FLJ hybrid joints, Compos. Part. B-Eng. 231 (2022) 109540, https://doi.org/10.1016/j.compositesb.2021.109540.

[25] Y. Wu, J. Lin, B.E. Carlson, P. Lu, M.P. Balogh, N.P. Irish, Y. Mei, Effect of laser ablation surface treatment on performance of adhesive-bonded aluminum alloys, Surf. Coat. Tech. 304 (2016) 340-347, https://doi.org/10.1016/j.surfcoat.2016.04.051.

[26] H. Bu, X. Li, B. Li, X. Li, X. Zhan, Enhanced interfacial joining strength of laser wobble joined 6061-T6 Al alloy/CFRTP joint via interfacial bionic textures pre-construction, Compos. Part. B-Eng. 261 (2023) 110787, https://doi.org/10.1016/j.compositesb.2023.110787.

[27] N. Saleema, D. Gallant, Atmospheric pressure plasma oxidation of AA6061-T6 aluminum alloy surface for strong and durable adhesive bonding applications, Appl. Surf. Sci. 282 (2013) 98-104, https://doi.org/10.1016/j.apsusc.2013.05.064.

[28] J. Červený, V. Novák, J. Kudláček, M. Sahul, O. Stejskal, Effect of pre-treatment of the surface of aluminum alloy on the properties of adhesive joints, Int. J. Adv. Manu. Tech. 137(9) (2025) 1-22, https://doi.org/ 10.1007/S00170-025-15318-Z.

[29] P. Pragathi, S.J. Jenison, K.A. Vijayan, G.R. Singh, K.V. Govindarajan, R. Sarathi, R.

Velmurugan, Enhanced interfacial bonding strength in K-300 adhesive joint between aluminum alloy and mild steel substrates through effective resin pre-coating treatment, Colloid. Surface. A. 687 (2024) 133491, https://doi.org/10.1016/j.colsurfa.2024.133491.

[30] F. Cheng, Y. Hu, X. Zhang, X. Hu, Z. Huang, Adhesive bond strength enhancing between carbon fiber reinforced polymer and aluminum substrates with different surface morphologies created by three sulfuric acid solutions, Compos. Part A-Appl. S. 146 (2021) 106427, https://doi.org/10.1016/j.compositesa.2021.106427.

[31] Y. Liu, M.A. Arenas, A.D. Frutos, J.D. Damborenea, A. Conde, P. Skeldon, G.E. Thompson, P. Bailey, T.C.Q. Noakes, Influence of nitric acid pre-treatment on Al–Cu alloys, Electrochim. Acta 53(13) (2008) 4454-4460, https://doi.org/10.1016/j.electacta.2008.01.026.

[32] S.G. Prolongo, A. Ureña, Effect of surface pre-treatment on the adhesive strength of epoxy–aluminium joints, Int. J. Adhes. Adhes. 29(1) (2009) 23-31, https://doi.org/10.1016/j.ijadhadh.2008.01.001.

[33] S. Joshi, W.G. Fahrenholtz, M.J. O'Keefe, Effect of alkaline cleaning and activation on aluminum alloy 7075-T6, Appl. Surf. Sci. 257(6) (2011) 1859-1863, https://doi.org/10.1016/j.apsusc.2010.08.126.

[34] S.D.L. Pierre, V. Giglia, M. Sangermano, L. Cornillon, O. Damiano, Etching of carbon fiber-reinforced plastics to increase their joint strength, J. Mater. Eng. Perform. 29 (2020) 242-250, https://doi.org/10.1007/s11665-020-04576-5.

[35] J. Li, Z. Liu, R. Zhang, G. Luo, Y. Sun, J. Zhang, Q. Shen, Surface treatment and solvent co-assisted easy direct bonding of polymer/metal, Mater. Design. 204 (2021) 109641, https://doi.org/10.1016/j.matdes.2021.109641.

[36] N. Banjo, T.T. Sasaki, K. Hono, Uniform formation of Ti-based conversion coatings on aluminum alloy surfaces by alkaline-acid etch treatment to improve organic coating properties, Appl. Surf. Sci. 661 (2024) 160005, https://doi.org/10.1016/j.apsusc.2024.160005.

[37] H. Senol, H. Ulus, C. Yildirim, A.A. Nadhari, S. Topal, M. Yildiz, Assessing fracture toughness performance of adhesively bonded carbon fiber/epoxy composite joints accompanied by acoustic emission inspection: Effect of surface treatment methods, Eng. Fract. Mech. 321 (2025) 111119, https://doi.org/10.1016/j.engfracmech.2025.111119.

[38] P. Molitor, V. Barron, T. Young, Surface treatment of titanium for adhesive bonding to polymer composites: a review, Int. J. Adhes. Adhes. 21(2) (2001) 129-136, https://doi.org/10.1016/S0143-7496(00)00044-0.

[39] G. Kang, W. Choi, A Study on the Effects of Surface Energy and Topography on the Adhesive Bonding of Aluminum Alloy, Korean J. Met. Mater. 59 (2021) 567–74, https://doi.org/10.3365/KJMM.2021.59.8.567.

[40] A.M. Pereira, J.M. Ferreira, F.V. Antunes, P.J. Bartolo, Study on the fatigue strength of AA 6082-T6 adhesive lap joints, Int. J. Adhes. Adhes. 29 (2009) 633–8, https://doi.org/10.1016/j.ijadhadh.2009.02.009.

[41] J. Zhang, X. Zhao, Y. Zuo, J. Xiong, The bonding strength and corrosion resistance of aluminum alloy by anodizing treatment in a phosphoric acid modified boric acid/sulfuric acid bath, Surf. Coat. Tech. 202(14) (2007) 3149-3156, https://doi.org/10.1016/j.surfcoat.2007.10.041.

[42] L. Dong, Y. Li, M. Huang, X. Hu, Z. Qu, Y. Lu, Effect of anodizing surface morphology on the adhesion performance of 6061 aluminum alloy, Int. J. Adhes. Adhes. 113 (2022) 103065,

https://doi.org/10.1016/j.ijadhadh.2021.103065.
[43] G.W. Critchlow, K.A. Yendall, D. Bahrani, A. Quinn, F. Andrews, Strategies for the replacement of chromic acid anodising for the structural bonding of aluminium alloys, Int. J. Adhes. Adhes. 26(6) (2006) 419-453, https://doi.org/10.1016/j.ijadhadh.2005.07.001.
[44] V. Fiore, F.F. Di, R. Miranda, M. Santamaria, D. Badagliacco, A. Valenza, Effects of anodizing surface treatment on the mechanical strength of aluminum alloy 5083 to fibre reinforced composites adhesive joints, Int. J. Adhes. Adhes. 108 (2021) 102868, https://doi.org/10.1016/j.ijadhadh.2021.102868.
[45] EN 485-2:2016, Aluminium and aluminium alloys-Sheet, strip and plate-Part 2: Mechanical properties, European Committee for Standardization, Brussels, 2016.
[46] ISO 527-2:2012, Plastics-Determination of tensile properties-Part 2: Test conditions for moulding and extrusion plastics, International Organization for Standardization, Geneva, 2012.
[47] Y.A. Kanani, Y. Liu, J.D. Hughes, J. Ye, X. Hou, Fracture mechanisms of hybrid adhesive bonded joints: effects of the stiffness of constituents, Int. J. Adhes. Adhes. 102 (2020) 102649, https://doi.org/10.1016/j.ijadhadh.2020.102649.
[48] A.Y. Kanani, X. Hou, J. Ye, A novel dissimilar single-lap joint with interfacial stiffness improvement, Compos. Struct. 252 (2020) 112741, https://doi.org/10.1016/j.compstruct.2020.112741.
[49] BS ISO 4587:2003, Adhesives-Determination of tensile lap-shear strength of rigid-to-rigid bonded assemblies, British Standards Institution, London, 2003.
[50] P. Galvez, J. Abenojar, M.A. Martinez, Effect of moisture and temperature on the thermal and mechanical properties of a ductile epoxy adhesive for use in steel structures reinforced with CFRP, Compos. Part. B-Eng. 176 (2019) 107194, https://doi.org/10.1016/j.compositesb.2019.107194.
[51] K. Pang, X. Wang, J. Ye, C. Carnegie, X. Hou, Effect of microstructural roughness on the performance and fracture mechanism of multi-type single lap joints, Compos. Part. B-Eng. 286 (2024) 111763, https://doi.org/10.1016/j.compositesb.2024.111763.
[52] Z. Ge, Q. Hu, K. Pang, Y. Zhu, X. Hou, Significantly improves the mechanical strength of aluminum alloy adhesive joint through electrochemical pre-treatment in environmentally friendly medium, J. Manuf. Process. 133 (2025) 592-606, https://doi.org/10.1016/j.jmapro.2024.11.082.
[53] P. Horodek, M.K. Eseev, A.G. Kobets, Studies of stainless steel exposed to sandblasting, Nukleonika 60 (2015) 721-724, https://doi.org/10.1515/nuka-2015-0129.
[54] S. Akpinar, A. Kars, S. Bayramoglu, M. Demiral, The influence of combination of surface roughness and nanostructure of adhesive on the strength of adhesively bonded joints, Int. J. Adhes. Adhes. 133 (2024) 103743, https://doi.org/10.1016/j.ijadhadh.2024.103743.
[55] J. Gao, W. Gu, F. Zhang, H. Geng, J. Zhong, L. Yao, Z. Zhao, J. Wang, Selective etching of Sr-modified and directionally solidified industrial Al–Si eutectic alloys for fabricating fibrous eutectic Si, Metals 11(12) (2021) 1974, https://doi.org/10.3390/met11121974.
[56] B. Qian, Z. Shen, Fabrication of superhydrophobic surfaces by dislocation-selective chemical etching on aluminum, copper, and zinc substrates, Langmuir 21(20) (2005) 9007-9009, https://doi.org/10.1021/LA051308C.
[57] S. Zhu, W. Deng, Y. Su, Recent advances in preparation of metallic superhydrophobic surface by chemical etching and its applications, Chinese J. Chem. Eng. 61 (2023) 221-236,

https://doi.org/10.1016/j.cjche.2023.02.018.
[58] K.J. Kubiak, M.C.T. Wilson, T.G. Mathia, P. Carval, Wettability versus roughness of engineering surfaces, Wear 271(3-4) (2011) 523-528, https://doi.org/10.1016/j.wear.2010.03.029.
[59] B. Wang, X. Hu, P. Lu, Improvement of adhesive bonding of grit-blasted steel substrates by using diluted resin as a primer, Int. J. Adhes. Adhes. 73 (2017) 92-99, https://doi.org/10.1016/j.ijadhadh.2016.11.012.
[60] Y. Hu, J. Zhang, L. Wang, H. Jiang, F. Cheng, X. Hu, A simple and effective resin pre-coating treatment on grinded, acid pickled and anodised substrates for stronger adhesive bonding between Ti-6Al-4V titanium alloy and CFRP, Surf. Coat. Tech. 432 (2022) 128072, https://doi.org/10.1016/j.surfcoat.2021.128072.
[61] P. Hirchenhahn, A.A. Sayyad, J. Bardon, A. Felten, P. Plapper;L. Houssiau, Highlighting chemical bonding between nylon-6.6 and the native oxide from an aluminum sheet assembled by laser welding, ACS Appl. Polym. Mater. 2 (2020) 2517-2527, https://doi.org/10.1021/acsapm.0c00015.
[62] H. Wan, J. Min, J. Lin, Experimental and theoretical studies on laser treatment strategies for improving shear bonding strength of structural adhesive joints with cast aluminum, Compos. Struct. 279 (2022) 114831, https://doi.org/10.1016/j.compstruct.2021.114831.
[63] I. Smoljko, S. Gudić, N. Kuzmanić, M. Kliškić, Electrochemical properties of aluminium anodes for Al/air batteries with aqueous sodium chloride electrolyte, J. Appl. Electrochem. 42(2012)969-977, https://doi.org/10.1007/s10800-012-0465-6.
[64] Y., Hu, B. Yuan, F. Cheng, X. Hu, NaOH etching and resin pre-coating treatments for stronger adhesive bonding between CFRP and aluminium alloy, Compos. Part. B-Eng. 178 (2019) 107478, https://doi.org/10.1016/j.compositesb.2019.107478.
[65] Y. Qiao, Y. Shin, J. Ramos, M.H. Engelhard, R.J. Seffens, D.R. Merkel, K.L. Simmons, Plasma treatment on both adhesive tape and adherends for significantly enhanced CFRTP-related adhesive joints, Appl. Surf. Sci. 649 (2024) 159092, https://doi.org/10.1016/j.apsusc.2023.159092.
[66] Y. Qiao, Y. Shin, M.R. Pallaka, E.K. Nickerson, D.R. Merkel, R.J. Seffens, A. Ortiz, J.L. Ramos, K.L. Simmons, Plasma surface modification coupled with thermal and step-over distance effects on significant fracture improvement of adhesively-bonded metal-CFRTP dissimilar materials, Compos. Sci. Technol. 232 (2023) 109833, https://doi.org/10.1016/j.compscitech.2022.109833.
[67] J. Comyn, Chapter 1 Theories of adhesion, Handbook Adhes. Sealants (2006) 21-50, https://doi.org/10.1016/S1874-5695(06)80012-6.